North Atlantic modulation of interdecadal variations in hot drought events over northeastern China

Huixin Li

Collaborative Innovation Center on Forecast and Evaluation of Meteorological Disasters/Key Laboratory of Meteorological Disasters, Ministry of Education/Joint International Research Laboratory of Climate and Environment Change, Nanjing University of Information Science & Technology, Nanjing, China

Nansen-Zhu International Research Centre, Institute of Atmospheric Physics, Chinese Academy of Sciences, Beijing, China

Shengping He

Geophysical Institute, University of Bergen and Bjerknes Centre for Climate Research, Bergen, Norway

Climate Change Research Center, Chinese Academy of Sciences, Beijing, China

Yongqi Gao

Nansen Environmental and Remote Sensing Center and Bjerknes Centre for Climate Research, Bergen, Norway

Nansen-Zhu International Research Center, Institute of Atmospheric Physics, Chinese Academy of Sciences, Beijing, China

Huopo Chen

Nansen-Zhu International Research Centre, Institute of Atmospheric Physics, Chinese Academy of Sciences, Beijing, China

Early Online Release: This preliminary version has been accepted for publication in *Journal of Climate*, may be fully cited, and has been assigned DOI 10.1175/JCLI-D-19-0440.1. The final typeset copyedited article will replace the EOR at the above DOI when it is published.

© 2020 American Meteorological Society

Collaborative Innovation Center on Forecast and Evaluation of Meteorological Disasters,
Nanjing University of Information Science & Technology, Nanjing, China

HUIJUN WANG

Collaborative Innovation Center on Forecast and Evaluation of Meteorological Disasters/Key Laboratory of Meteorological Disasters, Ministry of Education/Joint International Research Laboratory of Climate and Environment Change, Nanjing University of Information Science & Technology, Nanjing, China

Climate Change Research Center, Chinese Academy of Sciences, Beijing, China

Nansen-Zhu International Research Centre, Institute of Atmospheric Physics, Chinese Academy of Sciences, Beijing, China

Corresponding author: Chen Huopo

Address: Nansen-Zhu International Research Centre (NZC), Institute of Atmospheric Physics, Chinese Academy of Sciences, PO Box 9804, Beijing 100029, China

Email: chenhuopo@mail.iap.ac.cn

Accepted for publication in *Journal of Climate*. DOI10.1175/JCLI-D-19-0440.1.

ABSTRACT:

Based on the long-term reanalysis datasets and the multivariate copula method, this study reveals that the frequency of summer hot drought events (SHDEs) over northeastern China (NEC) shows interdecadal variations during 1925−2010. It is revealed that the summer sea surface temperature (SST) over the North Atlantic has a significant positive correlation with the frequency of SHDEs over NEC on the decadal time scale, indicating a potential influence of the Atlantic multidecadal oscillation (AMO). Further analyses indicate that during the positive phases of the AMO, the warming SST over the North Atlantic can trigger a stationary Rossby wave originating from the North Atlantic, which splits into two wave trains propagating along two different routes. One is a zonally orientated wave train that resembles the Silk Road pattern, whereas the other is an arching wave train that resembles the Polar/Eurasian pattern. A negative (positive) phase of the Silk Road pattern (Polar/Eurasian pattern) may result in the weakened westerly wind along the jet stream, the downward vertical motion, and the anomalous positive geopotential center over NEC, providing favorable conditions for precipitation deficiency and high temperature and resulting in increased SHDEs. Thus, the Silk Road pattern and the Polar/Eurasian pattern serve as linkages between the AMO and SHDEs over northeastern China in summer on the interdecadal time scale. Model simulations from CAM4 perturbed with warmer SST in the North Atlantic show precipitation deficiency and high temperature conditions over northeastern China in summer, supporting the potential impacts of the North Atlantic SST on SHDEs over northeastern China. The results suggest that

Accepted for publication in *Journal of Climate*. DOI10.1175/JCLI-D-19-0440.1.

the phase of the AMO should be taken into account in the decadal prediction of SHDEs over northeastern China in summer.

Accepted for publication in *Journal of Climate*. DOI10.1175/JCLI-D-19-0440.1.

1. Introduction

Drought is a natural disaster that can significantly affect the ecosystem, agriculture, and economy worldwide. Northeastern China is known as "the granary of China", which contributed one-fifth of the country's total grain production in 2017 (http://economy.caixin.com/2018-09-25/101329831.html). Agriculture in northeastern China is quite sensitive to changes in precipitation and temperature (Liu et al. 2018a). Previous studies have noted that summer drought events have great impacts on crop production and food security over northeastern China (Yu et al. 2014; Zheng et al. 2015). For instance, the extreme drought event in 2014 resulted in a serious decrease in agricultural production (approximately five billion kilograms) in northeastern China (http://news.cntv.cn/2014/08/26/ARTI1409032307435405.shtml). Recently, northeastern China suffered from another serious hot drought event in the summer of 2016, which led to a decrease in crop production and economic losses up to 15.61 billion yuan (Li et al. 2018a). Therefore, it is important for society to understand the mechanisms of drought events and to provide an early warning of such events.

Previous studies investigated the intensity of drought events over northeastern China mainly from the perspective of precipitation deficiency and found that summer precipitation over northeastern China varies among different time scales, including interannual variability (Sun and Wang 2012; Zhang et al. 2019), interdecadal variability (Han et al. 2015), and long-term trends (Liang et al. 2011). However, precipitation deficiency is not the only influential

Accepted for publication in *Journal of Climate*. DOI10.1175/JCLI-D-19-0440.1.

factor of the summer drought event. Although high temperatures and precipitation deficiency do not always occur simultaneously, it is worth noting that high temperatures accompanied by precipitation deficiency can aggregate the severity of drought events (e.g., drought events over California in 2014, Aghakouchak et al. 2014). Thus, it is important to investigate hot drought events characterized as simultaneous precipitation deficiencies and high temperatures. Actually, the summer hot drought events (SHDEs) over northeastern China became severe over the past half-century, and human activity may play an important role (Li et al. 2020). Recently, Li et al. (2018a) suggested a linkage between the interannual variations in SHDEs over northeastern China and the sea ice change in the Barents Sea in March after the late 1990s. However, no such linkage is detected for the period prior to 1996/97. Furthermore, the more frequent SHDEs over northeastern China after the late 1990s coincided with the interdecadal shift of the phase change of the Atlantic multidecadal oscillation (AMO).

The AMO is a mode of the natural variability of sea surface temperature (SST) occurring in the North Atlantic, which is characterized by basin-scale cooling or warming (Schlesinger and Ramankutty 1994). The AMO has a cycle of 60–80 years, but the drivers of the AMO remain unknown. A few studies suggested that the AMO is only a random variation that can be linked to intrinsic modes of atmospheric circulation (Deser et al. 2010; Amy et al. 2016), whereas other studies proposed that the large-scale ocean circulation (Knight et al. 2005) or the ocean-atmosphere coupling might contribute to these interdecadal variations (Omrani et al. 2014). Despite the fact that the mechanisms underlying the AMO are under debate, numerous

Accepted for publication in *Journal of Climate*. DOI10.1175/JCLI-D-19-0440.1.

studies have suggested that the interdecadal variations in the SST in the North Atlantic have great impacts on global climate changes. In summer, the AMO can influence the atmospheric circulation over the Atlantic (Semenov and Cherenkova 2018), North America and Europe (Sutton and Hodson 2005; Hu et al. 2011; Ionita et al. 2013; Kayano and Capistrano 2014; Ghosh et al. 2017), and Asia (Lu et al. 2006; Luo et al. 2017; Fan et al. 2018; Zhang et al. 2018). In winter, the AMO can influence Eurasian air temperature (Hao et al. 2016), the East Asian winter monsoon (Li and Bates 2007), and northeastern China winter precipitation (Han et al. 2018). In addition to its impact on precipitation, temperature, and monsoon systems, the AMO can also regulate the changes in Arctic sea ice (Li et al. 2018b), the intensity of the Aleutian–Icelandic low (Li et al. 2018c), the relationship between the North Atlantic Oscillation and the ENSO (Zhang et al. 2019), and the Walker circulation (Sun et al. 2017).

Recently, several studies found that the AMO is significantly correlated with drought events over several regions around the world. For instance, the AMO can modulate the impact of the ENSO on drought frequencies over the United States (Mo et al. 2009). In addition, the AMO can modulate the intensities of multiyear drought events over the Great Plains of North America, where the AMO accounts for approximately half a portion to influence the precipitation (Nigam et al. 2011). In addition, the influence of the AMO on interdecadal variations in drought frequency over the Yellow River became significant after the early 1990s, whereas it failed to produce the same influence before the 1990s (Qian et al. 2014). Hence, the question arises as to whether the interdecadal variations in SST over the North Atlantic can

Accepted for publication in *Journal of Climate*. DOI10.1175/JCLI-D-19-0440.1.

exert an influence on the interdecadal variations in SHDEs over northeastern China. An insight into these questions can help to understand the causal factors of the interdecadal changes in SHDEs over northeastern China and hence be conducive to reducing uncertainties in the future projection of the SHDEs over northeastern China.

The outline of the paper is as follows. Section 2 provides the datasets employed in this study and introduces the survival copula method and the wave activity flux method. Section 3 describes the characteristics of interdecadal changes in SHDEs over northeastern China. In section 4, the associated atmospheric circulations for more SHDEs over northeastern China are discussed. Section 5 further investigates the influence of the AMO-like pattern on the interdecadal variations in SHDEs over northeastern China. Discussion and conclusions are finally provided in section 6.

2. Data and methods

The monthly precipitation and surface air temperature datasets (version 4.01) derived from the Climatic Research Unit (CRU) are used in this research (Harris et al. 2014). The horizontal resolution of the CRU datasets is $0.25^{\circ}\times0.25^{\circ}$, covering the period 1901–2016. The monthly reanalysis datasets during the period 1900–2010 from ERA-20C are also employed, with a horizontal resolution of $2^{\circ}\times2^{\circ}$ (Poli et al. 2013). Variables, including meridional and zonal wind, surface-level pressure, geopotential height, air temperature, specific humidity, and vertical velocity, are used. The monthly reanalysis datasets of the downward solar radiation,

Accepted for publication in *Journal of Climate*. DOI10.1175/JCLI-D-19-0440.1.

the downward (upward) longwave radiation, the sensible heat net flux, and the latent heat net flux during the period 1900–2010 from 20th Century Reanalysis V2c data provided by the NOAA/OAR/ESRL PSD, Boulder, Colorado, USA (https://www.esrl.noaa.gov/psd/) are employed to calculate the net flux at the surface over northeastern China. In addition, the SST dataset during the period 1901–2016 from the Hadley Centre version 1 (HadISST1) is also employed (Balsamo et al. 2015), with a horizontal resolution of $1^{o}\times1^{o}$. In this research, northeastern China is defined within the region of 42–54°N and 110–135°E, and the summer is defined as the monthly mean of July to August (JA).

In the present study, the multivariate copula method is used to calculate the probability-based index (PI) that simultaneously considers precipitation deficiency and high temperature. The multivariate copula method has been widely used in recent studies (Michele et al. 2005; Salvadori and De Michele 2010; Zhang et al. 2013). To identify the vulnerable regions related to hot drought events (precipitation deficiency and high temperature), the joint survival function ($\bar{F_i}$) is introduced, which is defined as $\bar{F_i} = 1 - F_i$ (Salvadori et al. 2013). The definition of the joint survival cumulative distribution function (CDF) is defined as Eq. (1), which is based on the concept of the multivariate survival copula ($\hat{C}$) method (Salvadori et al. 2013)

$$PI = \hat{C}(\bar{F}_1(x_1), \bar{F}_2(x_2)) = P(X_1 > x_1, X_2 > x_2) \quad (1)$$

where x_1 and x_2 represent precipitation and temperature, and the CDFs of them are $F_1(x_1) = P(X_1 \leq x_1)$ and $F_2(x_2) = P(X_2 \leq x_2)$, respectively. The joint CDF for precipitation and

Accepted for publication in *Journal of Climate*. DOI10.1175/JCLI-D-19-0440.1.

temperature is calculated as $F(x_1, x_2) = \hat{C}(F_1(x_1), F_2(x_2))$ (Salvadori and De Michele 2010). Therefore, the marginal survival functions of precipitation ($\overline{F_1}(x_1) = P(X_1 > x_1)$) and temperature ($\overline{F_2}(x_2) = P(X_2 > x_2)$) are defined as PI-based on their joint survival CDFs ($\hat{C}(\bar{F}_1(x_1), \bar{F}_2(x_2)) = P(X_1 > x_1, X_2 > x_2)$) in equation (1). The PI varies between zero and unity, and the small values of the PI correspond to more severe hot drought events (Li et al. 2018a). In the present study, the interdecadal changes in short-term drought (summer) over NEC are investigated, and the small decadal values of the PI corresponds to more frequent SHDEs.

In terms of the propagation of wave trains, numerous studies have employed the concept of wave activity flux (WAF) (Wang and He 2015; Liu et al. 2018b; Sun and Wang 2018; Sun B. et al. 2019a). Here, we also calculate the WAF based on the method proposed by Takaya and Nakamura (2001) to investigate propagations of the stationary waves relating to SHDEs over northeastern China. Equation (2) gives the method to calculate the corresponding WAF, where W represents the three-dimensional wave flux, ψ is the stream function, $\mathrm{U} = (\bar{u}, \bar{v}, 0)^T$ denotes the basic flow, $\bar{u}$ and $\bar{v}$ are the climatological zonal and meridional wind components, respectively, p = (pressure/1000 hPa), a is the earth's radius, $N^2 = (R_a p^{\kappa}/H)(\partial\theta/\partial z)$ is the buoyancy frequency squared, and C_U is the vector indicating the phase propagation of U.

Accepted for publication in *Journal of Climate*. DOI10.1175/JCLI-D-19-0440.1.

$$W = \frac{p\cos\phi}{2|\mathrm{U}|}\begin{pmatrix} \frac{\overline{u}}{a^2\cos^2\phi}\left[\left(\frac{\partial\psi'}{\partial\lambda}\right)^2 - \psi'\frac{\partial^2\psi'}{\partial\lambda^2}\right] + \frac{\overline{v}}{a^2\cos^2\phi}\left[\frac{\partial\psi'}{\partial\lambda}\frac{\partial\psi'}{\partial\phi} - \psi'\frac{\partial^2\psi'}{\partial\lambda\partial\phi}\right] \\ \frac{\overline{u}}{a^2\cos^2\phi}\left[\frac{\partial\psi'}{\partial\lambda}\frac{\partial\psi'}{\partial\phi} - \psi'\frac{\partial^2\psi'}{\partial\lambda\partial\phi}\right] + \frac{\overline{v}}{a^2}\left[\left(\frac{\partial\psi'}{\partial\phi}\right)^2 - \psi'\frac{\partial^2\psi'}{\partial\phi^2}\right] \\ \frac{f_0^2}{N^2}\left\{\frac{\overline{u}}{a\cos\phi}\left[\frac{\partial\psi'}{\partial\lambda}\frac{\partial\psi'}{\partial z} - \psi'\frac{\partial^2\psi'}{\partial\lambda\partial z}\right] + \frac{\overline{v}}{a}\left[\frac{\partial\psi'}{\partial\phi}\frac{\partial\psi'}{\partial z} - \psi'\frac{\partial^2\psi'}{\partial\phi\partial z}\right]\right\} \end{pmatrix} + C_U M \quad (2)$$

Here, the Lanczos filtering method is used to extract the decadal signals with a 9-year low-pass filtered series by giving a symmetrical set of weights. In addition, Pearson's linear correlation coefficient is employed to conduct the statistical test. Considering that the 9-year low-pass filtered series substantially reduces the degree of freedom of the data, the effective degrees of freedom (N_e) is defined as in Eq. (3):

$$N_e = \frac{N}{1+2\sum_{i=1}^{10} a_i b_i} \quad (3)$$

where N is the length of the time series and a_i and b_i are the ith order autocorrelations for time series of a and b, respectively.

In this study, we identify a positive summer Polar/Eurasian pattern (POL) with regard to more SHDEs over northeastern China, which is characterized by an anomalous negative geopotential height over the polar region and an anomalous positive geopotential height over northeastern Asia. Here, the summer POL index is defined as the differences in geopotential height between the region of northeastern Asia (45–55°N, 90–125°E) and the polar region (65–80°N, 60–100°E) at 700 hPa in summer (Barnston and Livezey 1987). In addition, we also employ a Silk Road pattern index (SRPI), which is defined as the normalized principal component of the leading mode for 200 hPa meridional wind over East Asia (20–60°N, 30–130°E) in summer (Wang et al. 2017). The AMO index is defined as the 9-year low-pass filtered

Accepted for publication in *Journal of Climate*. DOI10.1175/JCLI-D-19-0440.1.

series of summer mean SST over the North Atlantic (0–65°N, 80°W–0°E) (Rayner 2003).

To confirm the proposed mechanisms, the sensitivity experiment based on the Community Atmospheric Model, version 4 (CAM4), is performed. Here, two numerical experiments, including a control run and a sensitivity experiment, are carried out. In the control run, the boundary condition is prescribed as the climatological monthly mean during the period 1981–2010. In the sensitivity experiment, we first calculate the anomalous composite SST over the North Atlantic in summer based on the negative and positive phases of the PINEC (the temporal series of the spatially averaged PI over northeastern China) from 1925 to 2010 (corresponding to the warming phases of the AMO-like pattern) (Fig. 6c). After that, the boundary condition of the SST in summer is set as the anomalous composite SST plus the boundary condition in the control run. For other months, the boundary conditions are prescribed as the climatological condition during 1981–2010. Both the control run and the sensitivity run are repeated 60 times, and we choose the last 40 ensembles for further analyses in this study. The horizontal resolution of CAM4 is 1.9^{o} latitude $\times 2.5^{o}$ longitude with 26 hybrid sigma-pressure levels. In this study, the differences between the sensitivity experiments and the control runs based on the relevant ensemble means are calculated to confirm the modulation of the summer AMO-like pattern on changes in SHDEs over northeastern China.

3. Decadal variations in summer hot drought events over northeastern China

Based on the multivariate survival method proposed in section 2, we calculate the PI to

Accepted for publication in *Journal of Climate*. DOI10.1175/JCLI-D-19-0440.1.

illustrate the interdecadal changes in SHDEs. During the past century, the PINEC exhibits interannual and interdecadal variations (Fig. 1a). Based on the 9-year low-pass filtered series (black line), two abrupt interdecadal changes in the PINEC during 1900–2016 are identified, which are around the mid-1950s (shift from negative to positive phase) and around the mid-1990s (shift from positive to negative phase). Generally, the abrupt decrease in the PINEC around the late 1990s is closely linked to the interdecadal decrease in summer precipitation (Han et al. 2015) and the abrupt increase in temperature (Chen and Lu 2014; Hong et al. 2017; Sun and Wang 2017) over northeastern China. In addition, the abrupt increase in the PINEC around the mid-1950s also coincided with the interdecadal decrease in temperature over northeastern China (figure not shown). Therefore, the interdecadal variations in the PINEC well represent the interdecadal variations in summer precipitation and temperature over northeastern China, which also show similarities to the interdecadal variations in the AMO index (Fig. 1b). It can be inferred that a positive (negative) phase of AMO may correspond to a negative (positive) phase of PINEC (the possible physical mechanisms are explained in section 5). However, this is not the case for 1905–1924. Namely, the negative phase of the AMO index was less significant during 1905–1924, while the PI was dominated as a positive anomaly during the negative phase of AMO for 1900–1914, accompanied by a large amplitude negative anomaly during 1915–1925 (Fig. 1a). Therefore, the relationship between the AMO index and PINEC was less robust during 1915–1925. To well demonstrate the out-phase relationship between AMO and PI, this study mainly focuses on the period 1925–2010 (results based on 1905–1924 are discussed in section 6). Based on the 9-year low-pass filtered PINEC

Accepted for publication in *Journal of Climate*. DOI10.1175/JCLI-D-19-0440.1.

series (Fig. 1b), the entire period is separated into three subperiods, P1 (1925–1954), P2 (1955–1995) and P3 (1996–2010), for composite analysis.

To investigate the spatial distributions of the summer surface temperature, precipitation, and PI across China with regard to the interdecadal variations in the summer PINEC, we present the corresponding regression maps in Fig. 2. Since the negative phase of the PI represents the condition of precipitation deficiency and high temperature, we multiply the PINEC by –1 to facilitate the analyses regarding hot drought events. Apparently, during the negative phases of the PINEC (more occurrences of SHDEs over northeastern China), there is an overall positive temperature anomaly over the northern part of China, especially over northeastern China, where the regression coefficients are significant at the 95% confidence level (Fig. 2a). In addition, precipitation deficiency is also observed over the northern part of China. For most grids over northeastern China, precipitation deficiency conditions are significant at the 95% confidence level (Fig. 2b). Influenced by precipitation deficiency and high temperature conditions, there is an obvious negative PI center over northeastern China where the regression coefficients are significant at the 95% confidence level (Fig. 2c). The results based on the composite analyses between the negative and the positive phases of the PINEC are similar (figures not shown).

For the summer PINEC, we also calculate the corresponding spatial distributions of explained variances based on the 9-year low-pass filtered datasets during the period 1925–2010. For the temperature (Fig. 2d) and PI (Fig. 2f), the explained variances are more than 80% for

Accepted for publication in *Journal of Climate*. DOI10.1175/JCLI-D-19-0440.1.

most of the grids over northeastern China. For precipitation, the explained variances over most of the grids of northeastern China are more than 50% (Fig. 2e). The results suggest that the interdecadal variations in the PINEC well explain the interdecadal variances in the summer surface air temperature, precipitation, and PI over northeastern China (all significant at the 95% confidence level).

Overall, changes in the PINEC can capture the spatial-temporal conditions of summer precipitation, temperature, and PI over northeastern China on the interdecadal timescale. In addition, the variances in summer precipitation, temperature, and PI over northeastern China can be highly explained by the PINEC on the interdecadal timescale. Accordingly, the PINEC is a good indicator to represent the interdecadal variations in SHDEs over northeastern China. In the following, the analyses regarding decadal changes in summer hot drought events over northeastern China are based on the 9-year low-pass filtered and detrended PINEC.

4. Anomalous atmospheric circulations for more summer hot drought events over northeastern China

To investigate the favorable atmospheric circulation patterns for the occurrences of SHDEs over northeastern China (corresponding to the negative phases of the PINEC) on the interdecadal timescale, Figure 3 displays the regression maps of the atmospheric circulations in summer with regard to the 9-year low-pass filtered PINEC during 1925–2010 after removing the linear trend.

Accepted for publication in *Journal of Climate*. DOI10.1175/JCLI-D-19-0440.1.

Corresponding to the negative phase of the PINEC, there is an anomalous anti-cyclonic center over northeastern China from low (Fig. 3d) to high (Fig. 3a) troposphere. Despite the climatological low level of specific humidity over northeastern China, the anomalous anti-cyclonic circulation favors water vapor transport (WVT) (Fig. S1a), which is unbeneficial to moisture accumulation (Fig. S1b) (Sun and Wang 2013). Additionally, an anomalous upper-level easterly wind along the jet core is present over northeastern China, weakening the intensity of and results in the northward movement of the westerly jet (see the dashed purple line in Fig. 3a). Previous studies suggested that the weakened upper-level westerly jet favors indirect circulation accompanied by the anomalous positive geopotential height over northeastern China (Chen et al. 2016; Hong and Lu 2016) from the sea level (Fig. 3e) to the mid (Fig. 3b) troposphere. In addition, at the nose of the upper-level jet stream, the air is deflected to the right side of the jet by the supergradient winds, leading to the descending motion on the right side (Brill et al. 1985). Associated with the positive geopotential height anomaly, a uniform descending motion (Fig. 3c) also exists over northeastern China, which further prevents moisture accumulation (Fig. S1) and cloud formation and leads to increased solar radiation (Fig. S2a) as well as positive surface net heat flux (Fig. 3f) over northeastern China. Accordingly, the increased surface net heat flux and the moisture deficiency lead to SHDEs. Therefore, the anomalous atmospheric circulations provide a favorable condition for more SHDEs over northeastern China, which is consistent with those features on the interannual time scales (Li et al. 2018a). Moreover, all of these results are consistent with the composite analysis between the negative and positive phases of the PINEC (figures not shown).

Accepted for publication in *Journal of Climate*. DOI 10.1175/JCLI-D-19-0440.1.

In addition to the regional atmospheric circulations over northeastern China, the teleconnection patterns also deserve attention (Li et al. 2018a). Corresponding to the negative phase of the PINEC, a positive Polar/Eurasian pattern that featured as an anomalous positive geopotential center is evident over northeastern China, with two anomalous negative geopotential centers to its north (polar region) and south (the southern part of China and the northwestern Pacific) (Fig. 4a). Being influenced by this teleconnection pattern, an anomalous anti-cyclonic center is evident over northeastern China, along with two anomalous cyclonic centers to its north and south sides (Fig. 4a). Meanwhile, the Silk Road pattern featured as a series of cyclonic and anticyclonic centers is also evident over the northern hemisphere (Fig. 4a). As suggested by the above analyses, the meridional displacement of the westerly jet that regulated by the Silk Road pattern is essential to influence atmospheric circulation over northeastern China (Hong and Lu, 2016). Subsequently, the influence of the Polar/Eurasian pattern and the Silk Road pattern on SHDEs are further investigated on the interdecadal time scale.

Figure 5a shows the 9-year low-pass filtered time series of the POL index, SRPI, and PI (calculated by the method proposed in section 2). Noticeably, the POL index (SRPI) is highly correlated with the PINEC (Fig. 5a), with a correlation coefficient of –0.64 (0.57) (both are significant at the 95% confidence level). Correspondingly, the anomalous summer atmospheric circulations with regard to the summer POL index (Figs. 5b–d) and SRPI (Figs. 5e–g) are also given. The results suggest that the positive (negative) phase of the Polar/Eurasian pattern (Silk

Accepted for publication in *Journal of Climate*. DOI10.1175/JCLI-D-19-0440.1.

Road pattern) is associated with an anomalous anti-cyclonic circulation (Figs. 5b, d, e, g) and a positive geopotential height (Figs. 5c, f) over northeastern China, and a weakened westerly jet (Figs. 5b, e), which indirectly leads to descending motion (figures not shown). As a result, during the negative phases of the PINEC, there is an anomalous positive Polar/Eurasian pattern (Fig. 4a) and a negative Silk Road pattern (Fig. 4a) over the northern hemisphere. Both of them induce favorable atmospheric circulations for precipitation deficiency and high temperature, which are further linked to more SHDEs over northeastern China (Figs. S3–S4).

5. Possible modulation of the summer sea surface temperature over the North Atlantic

Numerous studies have suggested that the interdecadal changes of the SST in the Atlantic, the Pacific, and the Indian Ocean may regulate the interdecadal climate variations globally (Zhu et al. 2011; Luo et al. 2018; Zhang et al. 2018; Sun B. et al. 2019b; Chen and Sun 2020). To investigate the causal factors for the interdecadal variations in SHDEs over northeastern China, we further focus on the associated variations in the global SST.

Figure 6 presents the global composite SST between different phases of the PINEC. Corresponding to the negative phases of the PINEC, there is an anomalous warming pattern over the North Atlantic and the Indo-Pacific sector and cooling over the Southern Ocean. The significant warming over the North Atlantic well resembles the positive phases of the AMO. Generally, the amplitude (coverage) of the positive SST anomalies in the North Atlantic is the largest (broadest) among the different oceans, regardless of the composite periods. For example,

Accepted for publication in *Journal of Climate*. DOI10.1175/JCLI-D-19-0440.1.

the anomalous positive SST in the North Atlantic reaches 0.4°C in most areas, significant at the 99% confidence level based on Student's *t*-test (Figs. 6a–c). However, only a few parts of the Indian Ocean and the South Pacific exhibit warming anomalies for case one (Fig. 6a). In comparison with the former case, the warming pattern over the Indian Ocean and the South Pacific seem to be more significant for case two (Fig. 6b), while the warming anomalies over these regions are no more than 0.2°C based on the case three (Fig. 6c). Accompanied by the warming SST over the North Atlantic, there are obvious ascending air over the North Atlantic at 700 hPa (Figs. 6d–f), suggesting an enhanced convective activity. Overall, the SST anomalies in the North Atlantic may be an important factor influencing the interdecadal variations in SHDEs over northeastern China.

Here, we define the SSTI as the spatially averaged SST over the North Atlantic (0–70°N, 70°W–25°E) (see the red rectangle in Fig. 6a) in summer. Figure 7a gives the 9-year low-pass filtered series of the SSTI and the PINEC during the period 1925–2010, with a correlation coefficient of –0.55 between them that significant at the 90% confidence level. The results suggest that the 9-year low-pass filtered series of the SSTI is nearly the same as the summer AMO index (Fig. 7b), with the correlation coefficient between the SSTI and the AMO index to be 0.98 (significant at the 99% confidence level). Hereafter, we use the AMO index to represent the interdecadal variations in the SST over the North Atlantic.

Figure 8 presents the anomalous atmospheric circulations with regard to the 9-year low-pass filtered AMO index in summer from 1925 to 2010. During the positive phases of the AMO,

Accepted for publication in *Journal of Climate*. DOI10.1175/JCLI-D-19-0440.1.

a positive Polar/Eurasian pattern and a negative Silk Road pattern are evident (Fig. 4b), accompanied by an anomalous anti-cyclonic (Figs. 8a, d) and positive geopotential center (Figs. 8b, e) over northeastern China. The weakened upper-level westerly wind along the jet over northeastern China is also obvious (Fig. 8a), which induces an anomalous descending motion (Fig. 8c) and a positive surface net heat flux over northeastern China (Fig. 8f). These anomalous atmospheric circulations benefit precipitation deficiency (Fig. 9b) and high temperature (Fig. 9a) over northeastern China, thus leading to more SHDEs (Fig. 9c).

It is interesting to note that the atmospheric anomaly pattern related to the AMO (Fig. 8) well resembles the pattern associated with the POL index (Fig. 5b–d) and the SPRI (Figs. 5e–g). Therefore, a hypothesis is proposed that the interdecadal variations in the AMO-like pattern might modulate the interdecadal variations in SHDEs over northeastern China and the associated atmospheric circulations through atmospheric teleconnection. As shown in Fig. 10, two routes of wave trains are identified over the mid to high latitudes during the negative phases of the PINEC, characterized by a series of anomalous negative and positive meridional wind centers (Fig. 10a) as well as anomalous anti-cyclonic and cyclonic centers (Fig. 4a). The wave train generally originates from the western North Atlantic, which propagates eastward and splits into two different parts over the eastern North Atlantic. In detail, one part is an arching wave train along the great circle route that propagates from the North Atlantic toward the polar region and further into northeastern Asia (resembling the Polar/Eurasian pattern), whereas the other part is a zonally orientated Rossby wave train propagating from the North Atlantic to East

Accepted for publication in *Journal of Climate*. DOI10.1175/JCLI-D-19-0440.1.

Asia (resembling the Silk Road pattern) (Fig. 10a). Moreover, there are anomalous upward wave trains generating over the western North Atlantic (approximately 70–50°W, 40°N–55°N) (Fig. 11a) and northern Atlantic (approximately 30–0°W, 60°N–80°N) (Fig. 11c) that propagate eastward, accompanied by a series of barotropic negative and positive meridional wind centers (Figs. 11a, c). In general, the warming over the North Atlantic (during the positive phase of AMO) releases more heat flux from the ocean to the atmosphere (consistent with Ghosh et al. 2017), which leads to enhanced convective activity (Fig. 6d–f) in the troposphere over the North Atlantic. The enhanced convective activity (Fig. 6d–f) generates a wave train over the North Atlantic (Li et al. 2008) and it propagates upward (Fig. 11b, d) and eastward (Fig. 10b), thus resulting in a series of meridional wind centers (Fig. 10b) as well as anti-cyclonic and cyclonic centers (Fig. 4b). Therefore, the positive phases of the AMO may modulate the formation and propagation of wave trains (Figs. 10b, 11b, 11d, and 4b) through air-sea interactions and convective activities (Fig. 6), which are further linked to atmospheric teleconnections related to SHDEs over northeastern China (Figs. 10a, 11a, 11c, and 4a).

The above results suggest that the two routes of wave trains are closely connected to SHDEs over northeastern China, characterized by an arching wave train (positive Polar/Eurasian pattern) and a zonally orientated wave train (negative Silk Road pattern). Therefore, the AMO account for the interdecadal variations in atmospheric teleconnections that further influence SHDEs over northeastern China. Here, we further investigate the role of the Polar/Eurasian pattern and the Silk Road pattern in regulating wave activities linked to SHDEs

Accepted for publication in *Journal of Climate*. DOI10.1175/JCLI-D-19-0440.1.

over northeastern China. The results suggest that the positive Polar/Eurasian pattern favors the arching wave train (Fig. 10c), while the negative Silk Road pattern favors the zonally orientated Rossby wave train (Fig. 10d) propagating from the eastern North Atlantic to East Asia. Therefore, the formation of a positive Polar/Eurasian pattern and a negative Silk Road pattern are the results of wave train propagation and atmospheric teleconnection relating to the positive phases of the AMO in summer, which are further linked to the negative phase of the PINEC (more SHDEs over northeastern China).

To further verify the above analyses, Figure 12 shows the simulated differences in East Asian atmospheric circulation between the sensitivity experiments and the control runs based on the ensemble means of CAM4. Corresponding to the warming North Atlantic (Fig. 13a), there is an anticyclone and positive geopotential center to the north of northeastern China (Figs. 12a, b), and both are further north compared with the reanalysis results (Figs. 7a, b). By contrast, the anticyclone at 700 hPa over northeastern China (Fig. 12c) shows high similarities to the reanalysis results (Fig. 7c) and hence provides an unfavorable condition for moisture accumulation. In addition, the jet stream is weakened by the easterly wind (Fig. 12a), which indirectly leads to descending motion over northeastern China (Fig. 12d). As a result, these anomalous atmospheric circulations result in warmer temperature (Fig. 13b) and less precipitation (Fig. 13c) over northeastern China, confirming the proposed linkage between the AMO and SHDEs over northeastern China (Fig. 8). In terms of the teleconnection patterns, two wave trains that propagate from the North Atlantic toward northeastern Asian are detected

Accepted for publication in *Journal of Climate*. DOI10.1175/JCLI-D-19-0440.1.

(Fig. S5a), accompanied by a series of anti-cyclonic and cyclonic centers (Fig. S5b). It should be noted that the teleconnections may be sensitive to the background flows in models as suggested by previous studies (Sun X. et al. 2019; Stephan et al. 2018); hence, CAM4 partially reproduce the Polar/Eurasian pattern and Silk Road pattern (Fig. S5).

6. Discussion and conclusions

In this study, the interdecadal variations in SHDE frequency over northeastern China are identified based on the multivariate probability-based index of the PINEC (Fig. 1). The results suggest that the negative (positive) values of the PINEC correspond to more (less) SHDEs over northeastern China (Fig. 2c), which well captures the conditions of precipitation, temperature, and SHDEs over northeastern China (Fig. 2). In terms of the associated regional atmospheric circulations with regard to more SHDEs over northeastern China, the weakened westerly along the jet stream is obvious (Fig. 3a) and hence induces indirect circulation characterized by an anomalous positive geopotential center (Fig. 3b) and a descending motion (Fig. 3c) over northeastern China.

Results suggest that the summer AMO-like pattern over the North Atlantic might account for the interdecadal variations in SHDE frequency over northeastern China. Generally, the decadal warming over the North Atlantic might excite anomalous wave activity over the North Atlantic through the air-sea interaction (Fig. 11b) and the enhanced convective activity (Fig. 6). The wave train originating from the western North Atlantic propagates eastward and splits

Accepted for publication in *Journal of Climate*. DOI10.1175/JCLI-D-19-0440.1.

into two different pathways (Fig. 10b). One of them is a zonally orientated Rossby wave train from the North Atlantic to East Asia, resembling the negative Silk Road pattern. The other is an arching wave train along the great circle route propagating from the North Atlantic to the polar region and further into East Asia, resembling the positive Polar/Eurasian pattern. Generally, these anomalous wave activities and atmospheric teleconnections are closely correlated to more SHDEs over northeastern China (Figs. 10a) by influencing the associated regional atmospheric circulations, featured as an anomalous anti-cyclonic center and positive geopotential center, a downward vertical motion, and a weakened upper-level westerly jet stream over northeastern China (Figs. 5, 8). These anomalous regional atmospheric circulations provide a favorable condition for precipitation deficiency (Fig. 9b) and high temperature (Fig. 9a), thus resulting in more SHDEs (Fig. 9c) over northeastern China. Consequently, interdecadal changes in the AMO may account for the interdecadal variations in SHDEs over northeastern China, and the Polar/Eurasian pattern and Silk Road pattern serve as pathways between the AMO and SHDEs over northeastern China.

While the results of this study suggest a potential linkage between the summer SST in the Atlantic Ocean and SHDEs over northeastern China on the interdecadal time scale, a few issues remain to be answered. The above analyses indicate that the relationship between the AMO and SHDEs is robust during 1925–2010, whereas it is not the case for 1905–1924 as suggested in section 3 (Fig. 1b). Therefore, a question is raised: whether the relationship between the AMO-PINEC through the Polar/Eurasian pattern and the Silk Road pattern also exists during

Accepted for publication in *Journal of Climate*. DOI10.1175/JCLI-D-19-0440.1.

1905–1924? To answer this question, the atmospheric circulation and wave activities associated with the AMO index during 1905–1924 are further analyzed. Results indicate that the Silk Road pattern is also evident (Fig. S6a) during 1905–1924, accompanied by the anomalous atmospheric teleconnections and wave activities (Fig. S6b). However, the Polar/Eurasian pattern was located northeastward during 1905–1924 compared to that during 1925–2010 (Fig. S6). Being influenced by the northeast-movement of the Polar/Eurasian pattern, the anticyclonic center and positive geopotential center (Fig. S7a, b, d), the positive net heat center (Fig. S7f), and the downward motion (Fig. S7c) consistently moved northeastward. These favorable atmospheric conditions for more SHDEs located to the northeastward of northeastern China. As a result, the SHDEs over northeastern China and the AMO is positively correlated during 1905–1924 (Fig. S8c) rather than negatively correlated during 1925–2010 (Fig. 9c), accompanied with the negatively (positively) correlation between the AMO and temperature (precipitation) over northeastern China (Figs. S8a, b). However, it should be noted that the relationship between the AMO and the SHDEs over northeastern China also existed during 1905–1914 (Fig. S8d), which indicates that this inconspicuous relationship is mainly influenced by the period of 1915–1924. In brief, the relationship between the AMO and the PINEC through Polar/Eurasian pattern and the Silk Road pattern did not exist during 1905–1924 (especially during 1915–1924), even though the Polar/Eurasian pattern and the Silk Road pattern were still evident during that period.

Actually, a previous study has suggested that the SST anomalies in the North Pacific,

Accepted for publication in *Journal of Climate*. DOI10.1175/JCLI-D-19-0440.1.

North Atlantic, and the Indian Ocean jointly modulate interdecadal variations of precipitation over eastern China (Zhang et al. 2018). Considering that anomalous warming is observed in the Indian Ocean and the western South Pacific corresponding to negative PINEC phases (Figs. 6a, b, c), the SSTs in the Indian Ocean and the western South Pacific might have an impact on the SHDEs over northeastern China. Thus, the role of SSTs in the Indian Ocean and the western South Pacific in the interdecadal variations of SHDEs deserves further attention.

In addition, the reliability of datasets should also be taken into consideration. The previous study has suggested that there is a large uncertainty of the data before 1920 in China due to the properties of the CRU material (Wang et al. 2015). According to the official statistical datasets (Lin et al. 1995), there are only 13–25 (37–42) stations across the whole China during 1905–1914 (1915–1920) and most of the them located in eastern China, while it increased significantly after 1920 (more than 100 stations). Therefore, the large uncertainty of datasets during 1905–1924 may also account for the inconspicuous relationship between AMO and PINEC during that period.

Our results suggest that the interdecadal change in SHDE frequency is partly a natural variability that is modulated by the AMO. If the AMO switches to a negative phase in the future, the number of SHDEs will likely be reduced given that the other climate forcings are unchanged.

Accepted for publication in *Journal of Climate*. DOI10.1175/JCLI-D-19-0440.1.

Acknowledgments

This research was supported by the National Key R&D Program of China (2016YFA0600701, 2018YFA0606403, 2017YFA0603804), the Major Program of the National Natural Science Foundation of China (41991283), the National Natural Science Foundation of China (Grants 41875118, 41605059, and 41505073), the CONNECTED supported by UTFORSK Partnership Program (UTF-2016-long-term/10030), the Young Talent Support Program by China Association for Science and Technology (Grant 2016QNRC001).

Accepted for publication in *Journal of Climate*. DOI 10.1175/JCLI-D-19-0440.1.

REFERENCES

Aghakouchak, A., L. Cheng, O. Mazdiyasni, and A. Farahmand, 2014: Global warming and changes in risk of concurrent climate extremes: Insights from the 2014 California drought. *Geophysical Research Letters*, **41,** 8847–8852, https://doi.org/10.1002/2014GL062308.

Amy, C., B. Katinka, L. N. Murphy, M. A. Cane, M. Thorsten, R. D. Gaby, and S. Bjorn, 2016: The Atlantic Multidecadal Oscillation without a role for ocean circulation. *Science*, **352,** 320–324, https://doi.org/10.1126/science.aab3980.

Balsamo, G., and Coauthors, 2015: ERA-Interim/Land: a global land surface reanalysis data set. *Hydrology & Earth System Sciences*, **19,** 389–407, https://doi.org/10.5194/hess-19-389-2015.

Barnston, A. G., and R. E. Livezey, 1987: Classification, Seasonality and Persistence of Low-Frequency Atmospheric Circulation Patterns. *Monthly Weather Review*, **115,** 1083–1126, https://doi.org/10.1175/1520-0493(1987)115<1083:csapol>2.0.co;2.

Brill, K., L. W. Uccellini, R. P. Burkhart, T. T. Warner, and R. A. Anthes, 1985: Numerical Simulations of a Transverse Indirect Circulation and Low-Level Jet in the Exit Region of an Upper-Level Jet. *Journal of the Atmospheric Sciences*, **42**, 1306–1320, https://doi.org/10.1175/1520-0469(1985)042<1306:NSOATI>2.0.CO;2.

Chen, P., and B. Sun, 2020: Improving the dynamical seasonal prediction of western Pacific warm pool sea surface temperatures using a physical-empirical model, *International*

Accepted for publication in *Journal of Climate*. DOI10.1175/JCLI-D-19-0440.1.

Journal of Climatology, https://doi.org/ 10.1002/joc.6481.

Chen, W., and R. Lu, 2014: A Decadal Shift of Summer Surface Air Temperature over Northeast Asia around the Mid-1990s. *Advances in Atmospheric Sciences*, **31,** 735–742, https://doi.org/10.1007/s00376-013-3154-4.

——, and Coauthors, 2016: Variation in Summer Surface Air Temperature over Northeast Asia and Its Associated Circulation Anomalies. *Advances in Atmospheric Sciences*, **33,** 1–9, https://doi.org/10.1007/s00376-015-5056-0.

Deser, C., M. A. Alexander, S. P. Xie, and A. S. Phillips, 2010: Sea surface temperature variability: patterns and mechanisms. *Annual Review of Marine Science*, **2,** 115–143, https://doi.org/10.1146/annurev-marine-120408-151453.

Fan, Y., K. Fan, Z. Xu, and S. Li, 2018: ENSO–South China Sea Summer Monsoon Interaction Modulated by the Atlantic Multidecadal Oscillation. *Journal of Climate*, **31,** 3061–3076, https://doi.org/10.1175/jcli-d-17-0448.1.

Ghosh, R., W. A. Müller, J. Baehr, and J. J. C. D. Bader, 2017: Impact of observed North Atlantic multidecadal variations to European summer climate: a linear baroclinic response to surface heating, *Climate Dynamics*, **48,** 3547–3563, https://doi.org/10.1007/s00382-016-3283-4.

Han, T., S. He, X. Hao, and H. Wang, 2018: Recent interdecadal shift in the relationship between Northeast China's winter precipitation and the North Atlantic and Indian Oceans.

Accepted for publication in *Journal of Climate*. DOI10.1175/JCLI-D-19-0440.1.

Climate Dynamics, **50,** 1413–1424, https://doi.org/10.1007/s00382-017-3694-x.

——, H. P. Chen, and H. J. Wang, 2015: Recent changes in summer precipitation in Northeast China and the background circulation. *International Journal of Climatology,* **35,** 4210–4219, https://doi.org/10.1002/joc.4280.

Hao, X., and S. He, and H. Wang, 2016: Asymmetry in the response of central Eurasian winter temperature to AMO. *Climate Dynamics,* **47,** 2139–2154, https://doi.org/10.1007/s00382-015-2955-9.

Harris, I., P. D. Jones, T. J. Osborn, and D. H. Lister, 2014: Updated high-resolution grids of monthly climatic observations - the CRU TS3.10 Dataset. *International Journal of Climatology*, **34,** 623–642, https://doi.org/doi:10.1002/joc.3711.

Hong, X., and R. Lu, 2016: The meridional displacement of the summer Asian jet, Silk Road Pattern, and tropical SST anomalies. *Journal of Climate*, **29,** 3753–3766, https://doi.org/10.1175/jcli-d-15-0541.1.

——, ——, and S. Li, 2017: Amplified summer warming in Europe–West Asia and Northeast Asia after the mid-1990s. *Environmental Research Letters*, **12,** 094007, https://doi.org/10.1088/1748-9326/aa7909.

Hu, Q. S., S. Feng, and R. J. Oglesby, 2011: Variations in North American Summer Precipitation Driven by the Atlantic Multidecadal Oscillation. *Journal of Climate*, **24**, 5555–5570, https://doi.org/10.1175/2011jcli4060.1.

Accepted for publication in *Journal of Climate*. DOI10.1175/JCLI-D-19-0440.1.

Ionita, M., N. Rimbu, S. Chelcea, and S. Patrut, 2013: Multidecadal variability of summer temperature over Romania and its relation with Atlantic Multidecadal Oscillation. *Theoretical and Applied Climatology*, **113,** 305–315, https://doi.org/10.1007/s00704-012-0786-8.

Kay, J. E., and Coauthors, 2015: The Community Earth System Model (CESM) Large Ensemble Project: A Community Resource for Studying Climate Change in the Presence of Internal Climate Variability. *Bulletin of the American Meteorological Society*, **96,** 1333–1349, https://doi.org/10.1175/bams-d-13-00255.1

Kayano, M. T., and V. B. Capistrano, 2014: How the Atlantic multidecadal oscillation (AMO) modifies the ENSO influence on the South American rainfall. *International Journal of Climatology*, **34,** 162–178, https://doi.org/10.1002/joc.3674.

Knight, J. R., R. J. Allan, C. K. Folland, M. Vellinga, and M. E. Mann, 2005: A Signature of Persistent Natural Thermohaline Circulation Cycles in Observed Climate. *Geophysical Research Letters*, **32,** 242–257, https://doi.org/10.1029/2005gl024233.

Li, F., Y. J. Orsolini, H. Wang, Y. Gao, and S. He, 2018a: Atlantic Multidecadal Oscillation modulates the impacts of Arctic sea ice decline. *Geophysical Research Letters*. **45**, 2497–2506, https://doi.org/10.1002/2017gl076210.

——, ——, ——, ——, ——, 2018b: Modulation of the Aleutian–Icelandic low seesaw and its surface impacts by the Atlantic Multidecadal Oscillation. *Advances in Atmospheric*

Accepted for publication in *Journal of Climate*. DOI10.1175/JCLI-D-19-0440.1.

Sciences, **35**, 95–105, https://doi.org/10.1007/s00376-017-7028-z.

Li, H., H. Chen, H. Wang, J. Sun, and J. Ma, 2018a: Can Barents Sea ice decline in spring enhance summer hot drought events over northeastern China? *Journal of Climate*, **31,** 4705–4725, https://doi.org/10.1175/jcli-d-17-0429.1.

——, ——, B. Sun, H. Wang, and J. Sun, 2020: A detectable anthropogenic shift toward intensified summer hot drought events over northeastern China. *Earth and Space Science*, https://doi.org/10.1029/2019EA000836.

Li, S., and G. T. Bates, 2007: Influence of the Atlantic Multidecadal Oscillation on the winter climate of East China. *Advances in Atmospheric Sciences*, **24,** 126–135, https://doi.org/10.1007/s00376-007-0126-6.

——, J. Perlwitz, X. Quan, and M. P. Hoerling, 2008: Modelling influence of North Atlantic multidecadal warmth on the Indian summer rainfall. *Geophysical Research Letters*, **35,** L05804, https://doi.org/10.1029/2007GL032901.

Liang, L., L. Li, and L. Qiang, 2011: Precipitation variability in Northeast China from 1961 to 2008. *Journal of Hydrology*, **404,** 67–76, https://doi.org/10.1016/j.jhydrol.2011.04.020.

Lin, X., S. Yu, and G. Tang, 1995: Temperature series of China in recent 100 years (in Chinese). *Scientia Atmospherica Sinica*, **19**, 525–534.

Liu, Y., H. Chen, H. Wang, and Y. Qiu, 2018b: The Impact of the NAO on the Delayed Break-Up Date of Lake Ice over the Southern Tibetan Plateau. *Journal of Climate*, **31,** 9073–

Accepted for publication in *Journal of Climate*. DOI10.1175/JCLI-D-19-0440.1.

9086, https://doi.org/10.1175/jcli-d-18-0197.1.

Liu, Z., Yang X., Lin X., Gowda P., Lv S., Wang J., 2018a: Climate zones determine where substantial increases of maize yields can be attained in Northeast China. *Climatic Change*, **149**, 473–487. https:// doi.org /article/10.1007/s10584-018-2243-x.

Lu, R., B. Dong, and H. Ding, 2006: Impact of the Atlantic Multidecadal Oscillation on the Asian summer monsoon. *Geophysical Research Letters,* **33,** 194–199, https://doi.org/doi:10.1029/2006gl027655.

Luo, F., S. Li, Y. Gao, N. Keenlyside, L. Svendsen, and T. Furevik, 2017: The connection between the Atlantic multidecadal oscillation and the Indian summer monsoon in CMIP5 models. *Climate Dynamics,* https://doi.org/10.1007/s00382-017-4062-6

——, ——, and T. Furevik, 2018: Weaker connection between the Atlantic Multidecadal Oscillation and Indian summer rainfall since the mid-1990s. *Atmospheric and Oceanic Science Letters,* **11(1)**, 37–43, https://doi.org/10.1080/16742834.2018.1394779.

Michele, C. D., G. Salvadori, M. Canossi, A. Petaccia, and R. Rosso, 2005: Bivariate Statistical Approach to Check Adequacy of Dam Spillway. *Journal of Hydrologic Engineering*, **10,** 50–57, https://doi.org/10.1061/(asce)1084-0699(2005)10:1(50).

Mo, K. C., J. K. E. Schemm, and S. H. Yoo, 2009: Influence of ENSO and the Atlantic multidecadal oscillation on drought over the United States. *Journal of Climate,* **22,** 5962–5982, https://doi.org/10.1175/2009jcli2966.1.

Accepted for publication in *Journal of Climate*. DOI10.1175/JCLI-D-19-0440.1.

Nigam, S., B. Guan, and A. Ruiz-Barradas, 2011: Key role of the Atlantic Multidecadal Oscillation in 20th century drought and wet periods over the Great Plains. *Geophysical Research Letters*, **38,** 239–255, https://doi.org/10.1029/2011gl048650.

Omrani, N. E., N. S. Keenlyside, J. Bader, and E. Manzini, 2014: Stratosphere key for wintertime atmospheric response to warm Atlantic decadal conditions. *Climate Dynamics*, **42,** 649–663, https://doi.org/10.1007/s00382-013-1860-3.

Poli, P., and Coauthors, 2013: The data assimilation system and initial performance evaluation of the ECMWF pilot reanalysis of the 20th-century assimilating surface observations only (ERA-20C). ERA Report Series 14, European Centre for Medium-Range Weather Forecasts, Reading, UK.

Qian, C., J. Y. Yu, and G. Chen, 2014: Decadal summer drought frequency in China: the increasing influence of the Atlantic Multi-decadal Oscillation. *Environmental Research Letters*, **9**, 124004, https://doi.org/10.1088/1748-9326/9/12/124004.

Quenouille, M. H., 1952: Associated Measurements. New York: Butterworths Scientific Publications, London and Academic Press, 242.

Rayner, N. A., 2003: Global analyses of sea surface temperature, sea ice, and night marine air temperature since the late nineteenth century. *Journal of Geophysical Research*, **108**, https://doi.org/10.1029/2002jd002670.

Salvadori, G., and C. De Michele, 2010: Multivariate multiparameter extreme value models and return periods: A copula approach. *Water Resources Research*, **46,** 219–233, https://doi.org/10.1029/2009wr009040.

——, F. Durante, and C. Michele, 2013: Multivariate return period calculation via survival functions. *Water Resources Research*, **49,** 2308–2311, https://doi.org/10.1002/wrcr.20204.

Schlesinger, M. E., and N. Ramankutty, 1994: An oscillation in the global climate system of period 65–70 years. *Nature*, **367,** 723–726, https://doi.org/10.1038/367723a0.

Semenov, V. A., and E. A. Cherenkova, 2018: Evaluation of the Atlantic Multidecadal Oscillation Impact on Large-Scale Atmospheric Circulation in the Atlantic Region in Summer. *Doklady Earth Sciences*, **478,** 263–267, https://doi.org/10.1134/s1028334x18020290.

Stephan, C., N. Klingaman, and A. Turner, 2018: A mechanism for the recently increased interdecadal variability of the Silk Road Pattern. *Journal of Climat*e, https://doi.org/10.1175/JCLI-D-18-0405.1.

Sun, B., and H. Wang, 2013: Water Vapor Transport Paths and Accumulation during Widespread Snowfall Events in Northeastern China. *Journal of Climate*, **26**, 4550–4566, https://doi.org/10.1175/JCLI-D-12-00300.1.

——, ——, 2017: A trend towards a stable warm and windless state of the surface weather conditions in northern and northeastern China during 1961–2014. *Advances in*

Accepted for publication in *Journal of Climate*. DOI10.1175/JCLI-D-19-0440.1.

Atmospheric Sciences, **34,** 713–726, https://doi.org/10.1007/s00376-017-6252-x.

——, ——, 2018: Enhanced connections between summer precipitation over the Three-River-Source region of China and the global climate system. *Climate Dynamics*, https://doi.org/10.1007/s00382-018-4326-9.

——, ——, and B. Zhou, 2019a: Climatic condition and synoptic regimes of two intense snowfall events in eastern China and implications for climate variability. *Journal of Geophysical Research: Atmospheres*, https://doi.org/10.1029/2018jd029921.

——, H. Li, and B. Zhou, 2019b: Interdecadal variation of Indian Ocean basin mode and the impact on Asian summer climate. *Geophysical Research Letters*, https://doi.org/10.1029/2019GL085019.

Sun, C., F. Kucharski, J. Li, F. F. Jin, I. S. Kang, and R. Ding, 2017: Western tropical Pacific multidecadal variability forced by the Atlantic multidecadal oscillation. *Nature Communications*, **8,** 15998, https://doi.org/10.1038/ncomms15998.

Sun, J., and H. Wang, 2012: Changes of the connection between the summer North Atlantic Oscillation and the East Asian summer rainfall. *Journal of Geophysical Research*, **117,** 393–407, https://doi.org/10.1029/2012jd017482.

Sun, X. Q., S. L. Li, X. W. Hong, and R. Y. Lu, 2019c: Simulated influence of the Atlantic Multidecadal Oscillation on summer Eurasian nonuniform warming since the mid-1990s. Adv. Atmos. Sci., 36(8), 811-822, https://doi.org/10.1007/s00376-019-8169-z.

Accepted for publication in *Journal of Climate*. DOI 10.1175/JCLI-D-19-0440.1.

Sutton, R. T., and D. L. R. Hodson, 2005: Atlantic Ocean Forcing of North American and European Summer Climate. *Science*, **309,** 115–118, https://doi.org/10.1126/science.1109496.

Takaya, K., and H. Nakamura, 2001: A Formulation of a Phase-Independent Wave-Activity Flux for Stationary and Migratory Quasigeostrophic Eddies on a Zonally Varying Basic Flow. *Journal of the Atmospheric Sciences*, **58,** 608–627, https://doi.org/10.1175/1520-0469(2001)058<0608:afoapi>2.0.co;2.

Wang, H., and S. He, 2015: The North China/Northeastern Asia Severe Summer Drought in 2014. *Journal of Climate*, **28,** 6667–6681, https://doi.org/10.1175/jcli-d-15-0202.1.

Wang, L., P. Xu, W. Chen, and Y. Liu, 2017: Interdecadal Variations of the Silk Road Pattern. *Journal of Climate*, **30,** 9915–9932, https://doi.org/10.1175/jcli-d-17-0340.1.

Wang, Z., Y. Li, S. Wang, J. Feng, and J. Wang, 2015: Characteristics of drought at multiple time scales in the east of northwest China from 1901 to 2012 (in Chinese). *Journal of Desert Research*, **35**, 1666–1673, https://doi.org/10.7522/j.issn.1000–694X.2014.00190.

Yu, X., X. He, H. Zheng, R. Guo, Z. Ren, Z. Dan, and J. Lin, 2014: Spatial and temporal analysis of drought risk during the crop-growing season over northeast China. *Natural Hazards*, **71,** 275–289, https://doi.org/10.1007/s11069-013-0909-2.

Zhang, J., H. Chen, and S. Zhao, 2019: A tripole pattern of summertime rainfall and the teleconnections linking northern China to the Indian subcontinent. *Journal of Climate*,

Accepted for publication in *Journal of Climate*. DOI10.1175/JCLI-D-19-0440.1.

32, 3637–3652, https://10.1175/JCLI-D-18-0659.1.

Zhang, Q., J. F. Li, V. P. Singh, and C. Y. Xu, 2013: Copula-based spatio-temporal patterns of precipitation extremes in China. *International Journal of Climatology*, **33,** 1140–1152, https://doi.org/10.1002/joc.3499.

Zhang, W., X. Mei, X. Geng, A. G. Turner, and F. F. Jin, 2019: A Nonstationary ENSO–NAO Relationship Due to AMO Modulation. *Journal of Climate*, **32,** 33–43, https://doi.org/10.1175/jcli-d-18-0365.1.

Zhang, Z., X. Sun, and X. Q. Yang, 2018: Understanding the Interdecadal Variability of East Asian Summer Monsoon Precipitation: Joint Influence of Three Oceanic Signals, *Journal of Climate*, **31,** 5485–5506, https://doi.org/10.1175/jcli-d-17-0657.1.

Zheng, H., G. Shen, X. He, X. Yu, Z. Ren, and Z. Dan, 2015: Spatial assessment of vegetation vulnerability to accumulated drought in Northeast China. *Regional Environmental Change*, **15,** 1639–1650, https://doi.org/10.1007/s10113-014-0719-4.

Zhu, Y., H. Wang, W. Zhou, and J. Ma, 2011: Recent changes in the summer precipitation pattern in East China and the background circulation. *Climate Dynamics*, **36,** 1463–1473, https://doi.org/10.1007/s00382-010-0852-9.

Accepted for publication in *Journal of Climate*. DOI10.1175/JCLI-D-19-0440.1.

Figure Captions

FIG. 1. (a) Temporal series of the anomalous probability-based index (PI) averaged over northeastern China (NEC; 42°–54°N, 110°–135°E) in summer (JA; July to August) during 1900 to 2016 after removing linear trend. The black line denotes the corresponding 9-year low-pass filtered series using the Lanczos filter method. (b) Time series of 9-year low-pass filtered anomalous PINEC (blue) and the AMO index from 1905 to 2010 after removing the linear trend.

FIG. 2. Regression maps of the 9-year low-pass filtered (a) surface air temperature (°C), (b) precipitation (mm), and (c) PI in JA with regard to 9-year low-pass filtered PI series averaged over NEC (PINEC) in JA during the period from 1925 to 2010 after removing linear trend. The variance for 9-year low-pass filtered (d) surface air temperature (%), (e) precipitation (%), and (f) PI (%) in JA explained by PINEC based on 9-year low-pass filtered datasets from 1925 to 2010 after removing linear trend. Stippling denotes the regression coefficient or the explained variances significant at the 95% confidence level based on the Student's *t*-test. Here, PINEC is multiplied by –1.

FIG. 3. Regression maps of the 9-year low-pass filtered circulations in JA with regard to 9-year filtered PINEC in JA from 1925 to 2010 after removing linear trend: (a) 200 hPa (m s^{-1}) and (d) 700 hPa wind (m s^{-1}), (b) 500 hPa geopotential height (gpm), (c) vertical–horizontal cross-section averaged along 115°–135 °E (m s^{-1}), (e) sea level pressure (Pa), and (f) net heat flux (W

Accepted for publication in *Journal of Climate*. DOI10.1175/JCLI-D-19-0440.1.

m^{-2}). The dashed purple line in (a) gives the climatological position of the jet stream. Blue shading in (a), (c) and stippling in (b), (e), and (f) denote the regression coefficient significant at the 90% confidence level based on the Student's *t*-test. Here, the zonal mean of geopotential height in (b) and (e) is removed, and PINEC is multiplied by –1.

FIG. 4. Regression maps of the 9-year low-pass filtered 300 hPa wind (arrow, units: m s^{-1}) and meridional wind (shading, units: m s^{-1}) with regard to (a) 9-year filtered PINEC and (b) 9-year filtered AMO index. Red arrows denote the anomalies significant at the 90% confidence level based on the Student's *t*-test. Here, PINEC is multiplied by –1.

FIG. 5. (a) Time series of 9-year low-pass filtered anomalous PINEC (grey shading), POL index (red line), and SRPI index (blue line) from 1925 to 2010 after removing linear trend. (b)–(d) are the same as FIG. 3(a), (b), and (d), but for the results regard to 9-year filtered POL index. (e)–(g) are the same as FIG. 3(a), (b), and (d), but for the results regard to 9-year filtered SRPI index. Here, SRPI is multiplied by –1.

FIG. 6. Globally composite sea surface temperature (SST) in summer during the period between (a) P1 (1925–1954) and P2 (1955–1995) (case one) (^{o}C), (b) P3 (1996–2010) and P2 (1955–1995) (case two) (^{o}C), and (c) P1+P3 and P2 (case three) (^{o}C) after removing linear trend. (d)–(f) are the same as (a)–(c), but for 700 hPa ω over North Atlantic (units: m s^{-1}). Stippling denotes the anomalies significant at the 90% confidence level based on the Student's *t*-test. The red rectangle indicates the North Atlantic.

FIG. 7. (a) Time series of 9-year low-pass filtered anomalous PINEC and the SSTI index from

Accepted for publication in *Journal of Climate*. DOI 10.1175/JCLI-D-19-0440.1.

1925 to 2010 after removing the linear trend. (b) Time series of 9-year low-pass filtered anomalous summer SSTI and the AMO index from 1905 to 2012 after removing linear trend.

FIG. 8. Same as FIG. 3, but for the results with regard to the 9-year low-pass filtered AMO index in JA from 1925 to 2010 after removing the linear trend.

FIG. 9. Same as FIG. 2, but for the results regarding the 9-year low-pass filtered AMO index in JA from 1925 to 2010 after removing the linear trend. Stippling denotes the regression coefficient or the explained variances significant at the 90% confidence level based on the Student's *t*-test.

FIG. 10. Regression maps of 9-year low-pass filtered 300 hPa meridional wind anomalies (shading) and wave activity flux (vector; units: $m^2\ s^{-2}$) in JA with regard to 9-year filtered (a) PINEC, (b) AMO index, (c) POL index, and (d) SRPI index during 1925–2010 after removing linear trend. Stippling denotes the anomalies significant at the 90% confidence level based on the Student's *t*-test. Here, PINEC is multiplied by –1.

FIG. 11. Regression maps of 9-year low-pass filtered vertical-horizontal cross-section averaged along 40°N–55°N for JA wave flux (vectors, units: $m\ s^{-1}$) and meridional wind (shading, units: $m\ s^{-1}$) anomalies with regard to (a) 9-year filtered PINEC and (b) 9-year filtered AMO index. Regression maps of 9-year low-pass filtered vertical-horizontal cross-section averaged along 60°N–80°N for JA wave flux (vectors, units: $m\ s^{-1}$) and meridional wind (shading, units: $m\ s^{-1}$) anomalies with regard to (c) 9-year filtered PINEC and (d) 9-year filtered AMO index. Stippling denotes the anomalies significant at the 90% confidence level significant based on

Accepted for publication in *Journal of Climate*. DOI10.1175/JCLI-D-19-0440.1.

the Student's *t*-test. Here, PINEC is multiplied by –1.

FIG. 12. Composite differences of (a) 200 hPa wind (units: m s^{-1}), (b) 500 hPa geopotential height (units: gpm), (c) 700 hPa wind (units: m s^{-1}), and (d) vertical–horizontal cross-section averaged along 115°–135 °E (units: m s^{-1}) between sensitive runs and control experiments based on 40 ensembles. Colored arrow in (a, c) and stippling in (b) denote that more than half of the models share the same sign as the ensemble mean. The dashed purple line in (a) gives the climatological position of the jet stream. Here, the zonal mean of geopotential height in (b) is removed.

FIG. 13. Composite differences of (a) SST (units: °C), (b) surface air temperature (units: °C), and (c) precipitation (units: mm) between sensitive runs and control experiments based on the ensembles means of the 40 ensembles. Stippling in (b, c) denotes that more than half of the ensembles share the same sign as the ensemble mean.

Accepted for publication in *Journal of Climate*. DOI10.1175/JCLI-D-19-0440.1.

Figures

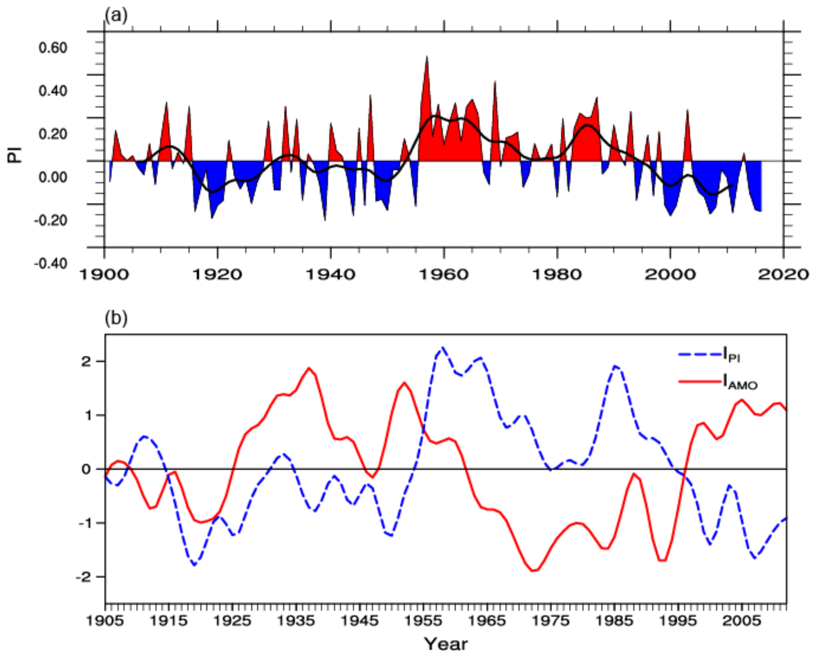

FIG. 1. (a) Temporal series of the anomalous probability-based index (PI) averaged over northeastern China (NEC; 42°–54°N, 110°–135°E) in summer (JA; July to August) during 1900 to 2016 after removing linear trend. The black line denotes the corresponding 9-year low-pass filtered series using the Lanczos filter method. (b) Time series of 9-year low-pass filtered anomalous PINEC (blue) and the AMO index from 1905 to 2010 after removing the linear trend.

Accepted for publication in *Journal of Climate*. DOI10.1175/JCLI-D-19-0440.1.

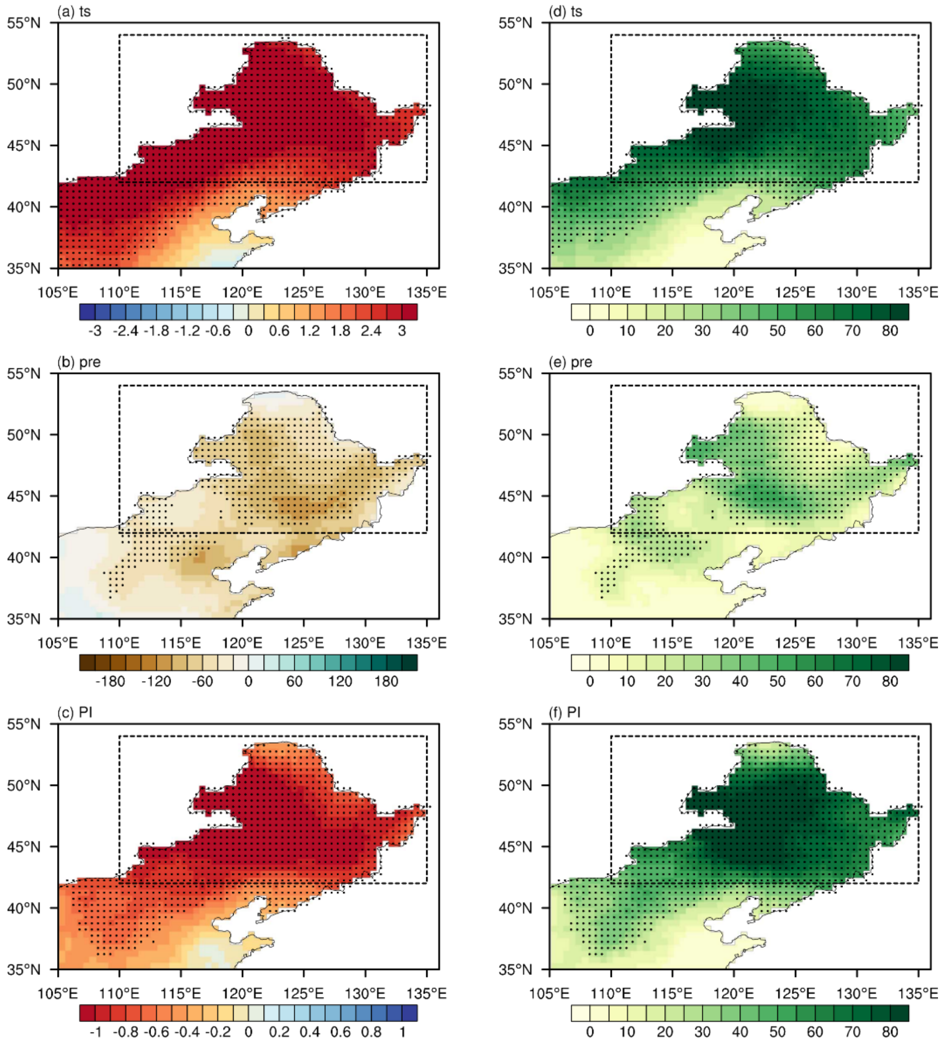

FIG. 2. Regression maps of the 9-year low-pass filtered (a) surface air temperature (°C), (b) precipitation (mm), and (c) PI in JA with regard to 9-year low-pass filtered PI series averaged over NEC (PINEC) in JA during the period from 1925 to 2010 after removing linear trend. The variance for 9-year low-pass filtered (d) surface air temperature (%), (e) precipitation (%), and (f) PI (%) in JA explained by PINEC based on 9-year low-pass filtered datasets from 1925 to 2010 after removing linear trend. Stippling denotes the regression coefficient or the explained variances significant at the 95% confidence level based on the Student's *t*-test. Here, PINEC is multiplied by –1.

Accepted for publication in *Journal of Climate*. DOI10.1175/JCLI-D-19-0440.1.

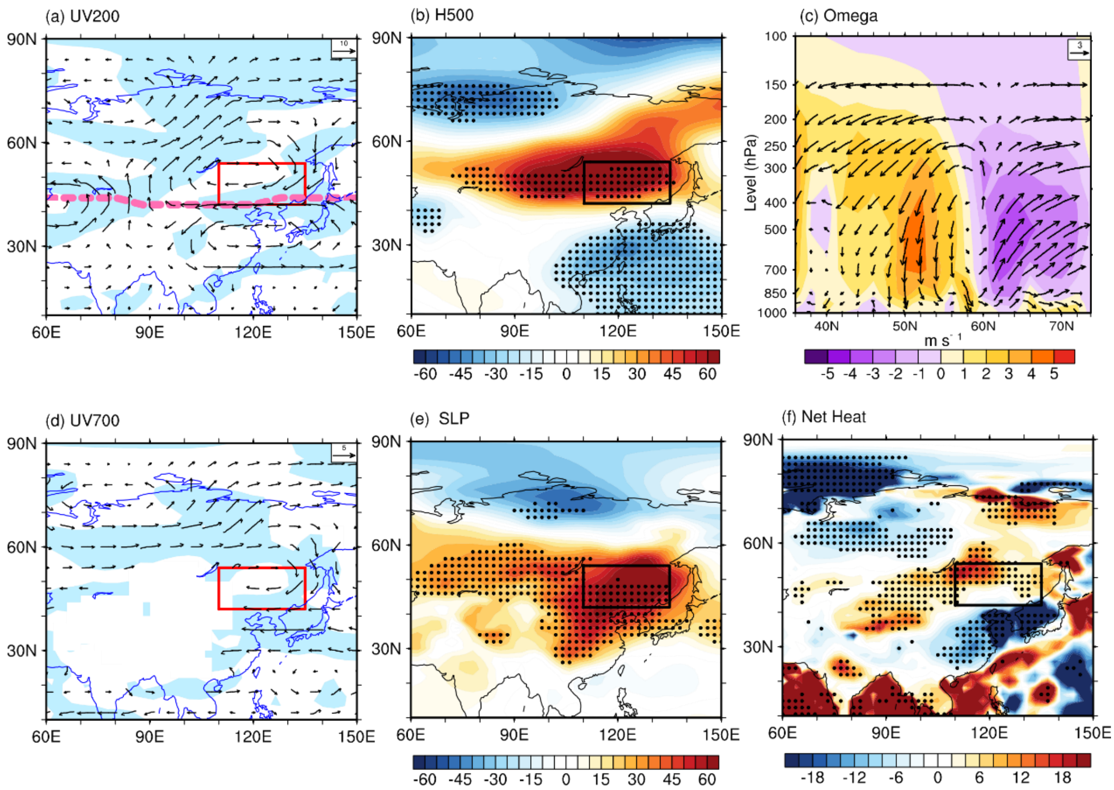

FIG. 3. Regression maps of the 9-year low-pass filtered circulations in JA with regard to 9-year filtered PINEC in JA from 1925 to 2010 after removing linear trend: (a) 200 hPa (m s^{-1}) and (d) 700 hPa wind (m s^{-1}), (b) 500 hPa geopotential height (gpm), (c) vertical–horizontal cross-section averaged along 115º–135 ºE (m s^{-1}), (e) sea level pressure (Pa), and (f) net heat flux (W m^{-2}). The dashed purple line in (a) gives the climatological position of the jet stream. Blue shading in (a), (c) and stippling in (b), (e), and (f) denote the regression coefficient significant at the 90% confidence level based on the Student's *t*-test. Here, the zonal mean of geopotential height in (b) and (e) is removed, and PINEC is multiplied by –1.

Accepted for publication in *Journal of Climate*. DOI10.1175/JCLI-D-19-0440.1.

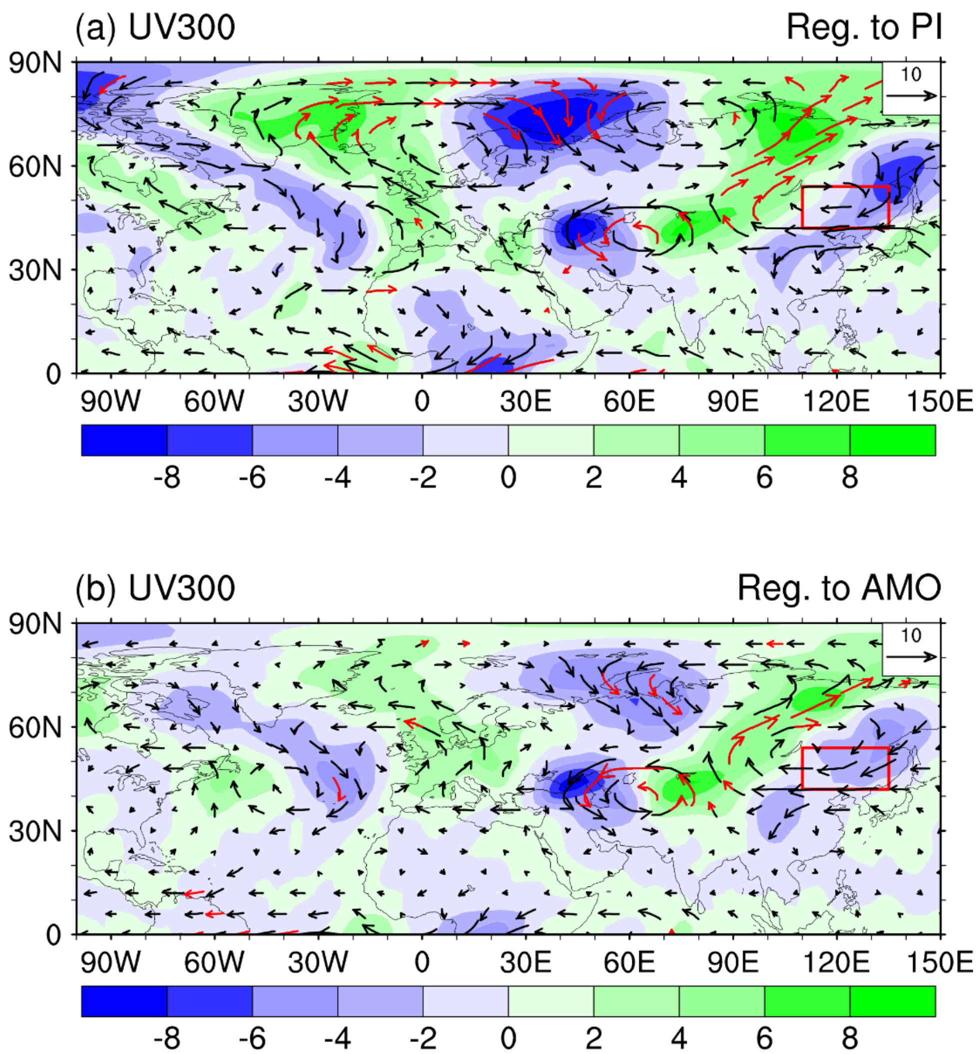

FIG. 4. Regression maps of the 9-year low-pass filtered 300 hPa wind (arrow, units: m s^{-1}) and meridional wind (shading, units: m s^{-1}) with regard to (a) 9-year filtered PINEC and (b) 9-year filtered AMO index. Red arrows denote the anomalies significant at the 90% confidence level based on the Student's *t*-test. Here, PINEC is multiplied by –1.

Accepted for publication in *Journal of Climate*. DOI10.1175/JCLI-D-19-0440.1.

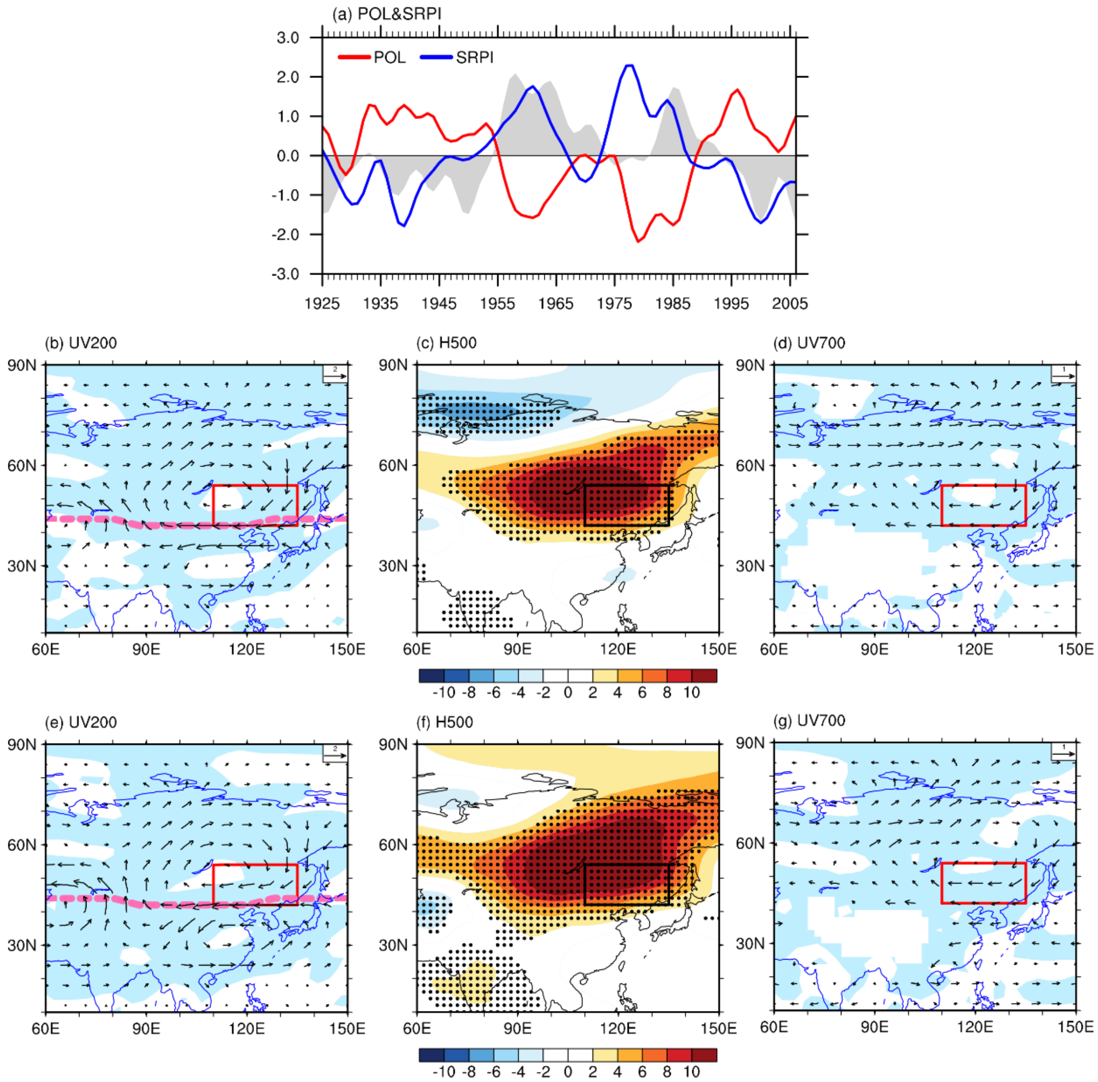

FIG. 5. (a) Time series of 9-year low-pass filtered anomalous PINEC (grey shading), POL index (red line), and SRPI index (blue line) from 1925 to 2010 after removing linear trend. (b)–(d) are the same as FIG. 3(a), (b), and (d), but for the results regard to 9-year filtered POL index. (e)–(g) are the same as FIG. 3(a), (b), and (d), but for the results regard to 9-year filtered SRPI index. Here, SRPI is multiplied by –1.

Accepted for publication in *Journal of Climate*. DOI10.1175/JCLI-D-19-0440.1.

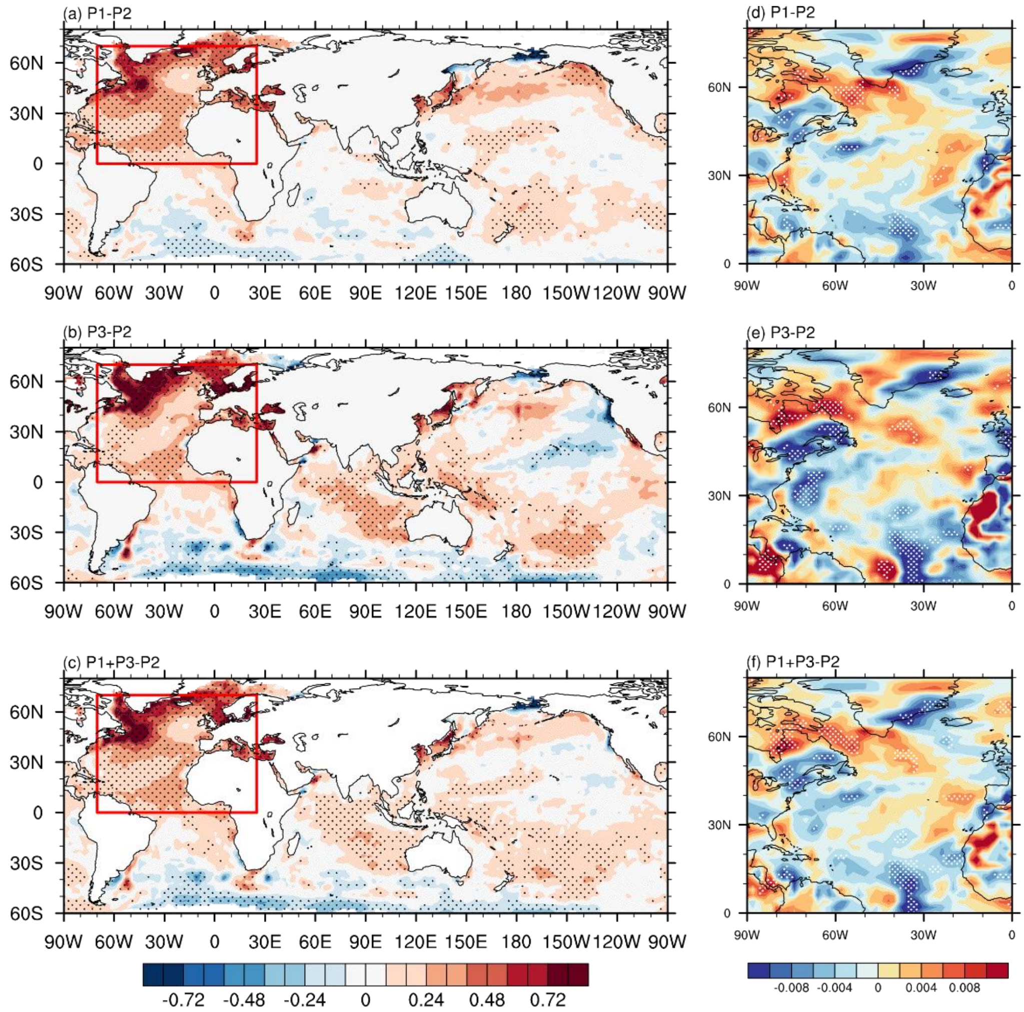

FIG. 6. Globally composite sea surface temperature (SST) in summer during the period between (a) P1 (1925–1954) and P2 (1955–1995) (case one) (°C), (b) P3 (1996–2010) and P2 (1955–1995) (case two) (°C), and (c) P1+P3 and P2 (case three) (°C) after removing linear trend. (d)–(f) are the same as (a)–(c), but for 700 hPa ω over North Atlantic (units: m s^{-1}). Stippling denotes the anomalies significant at the 90% confidence level based on the Student's *t*-test. The red rectangle indicates the North Atlantic.

Accepted for publication in *Journal of Climate*. DOI10.1175/JCLI-D-19-0440.1.

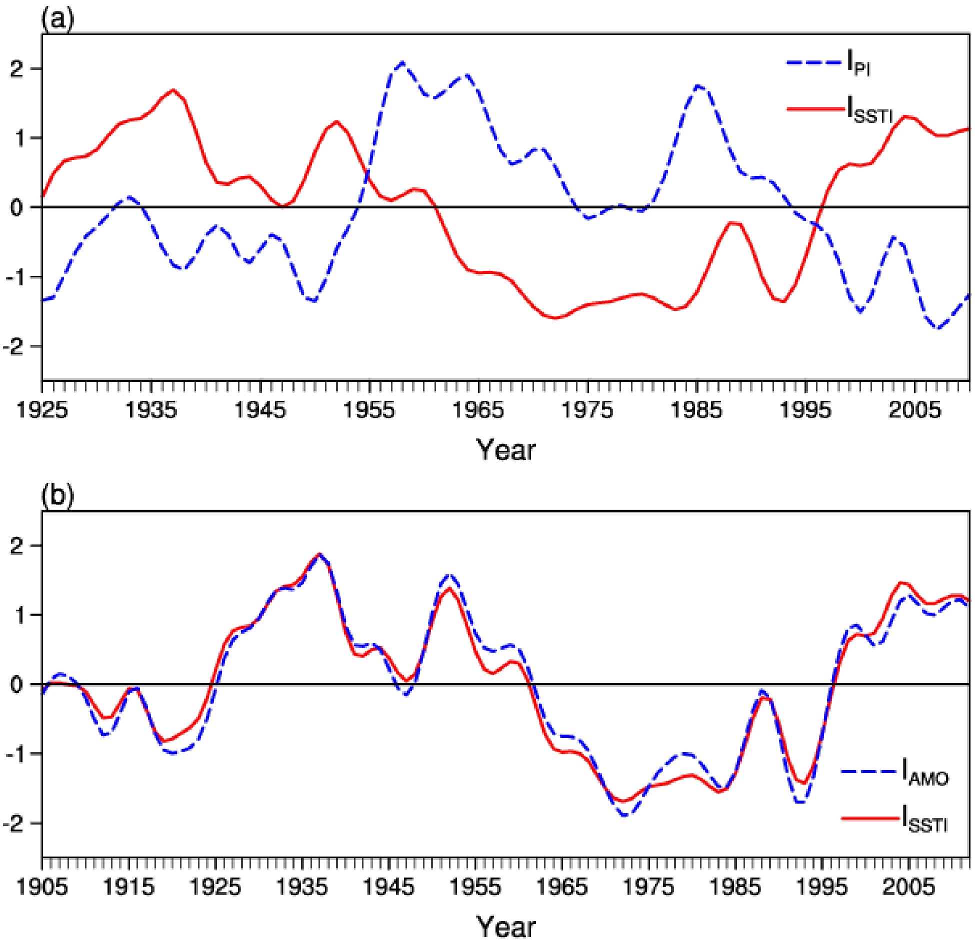

FIG. 7. (a) Time series of 9-year low-pass filtered anomalous PINEC and the SSTI index from 1925 to 2010 after removing the linear trend. (b) Time series of 9-year low-pass filtered anomalous summer SSTI and the AMO index from 1905 to 2012 after removing linear trend.

Accepted for publication in *Journal of Climate*. DOI10.1175/JCLI-D-19-0440.1.

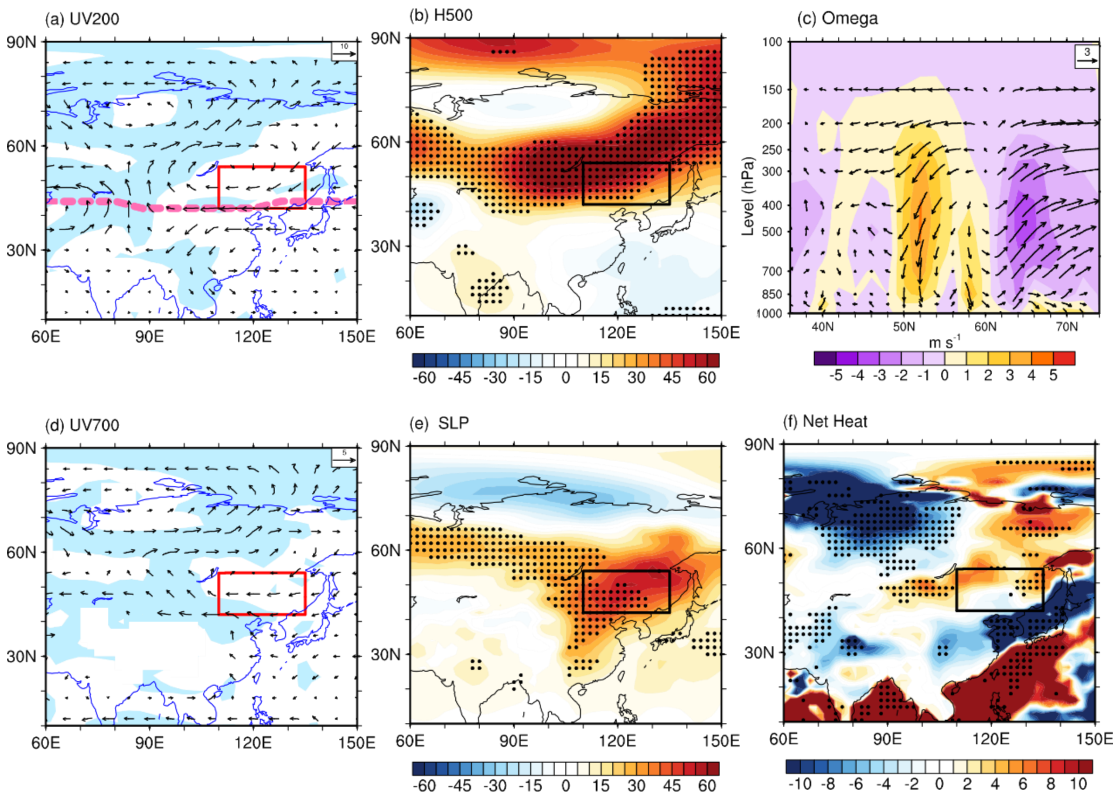

FIG. 8. Same as FIG. 3, but for the results with regard to the 9-year low-pass filtered AMO index in JA from 1925 to 2010 after removing the linear trend.

Accepted for publication in *Journal of Climate*. DOI10.1175/JCLI-D-19-0440.1.

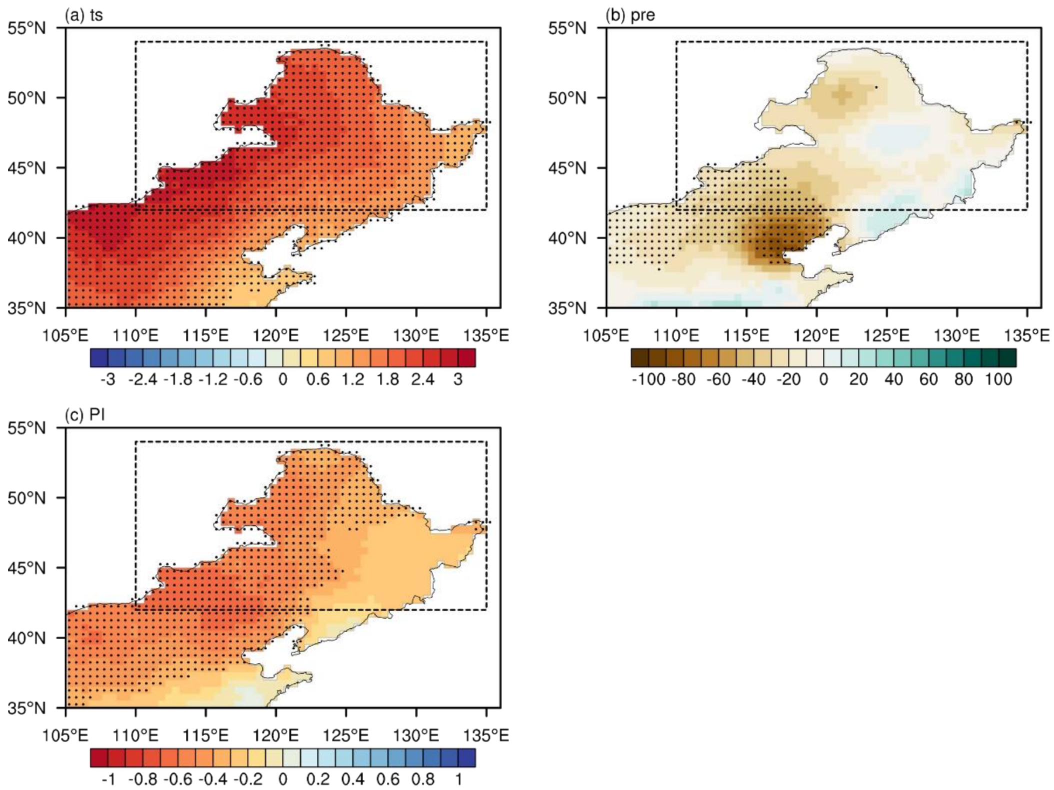

FIG. 9. Same as FIG. 2, but for the results regarding the 9-year low-pass filtered AMO index in JA from 1925 to 2010 after removing the linear trend. Stippling denotes the regression coefficient or the explained variances significant at the 90% confidence level based on the Student’s *t*-test.

Accepted for publication in *Journal of Climate*. DOI10.1175/JCLI-D-19-0440.1.

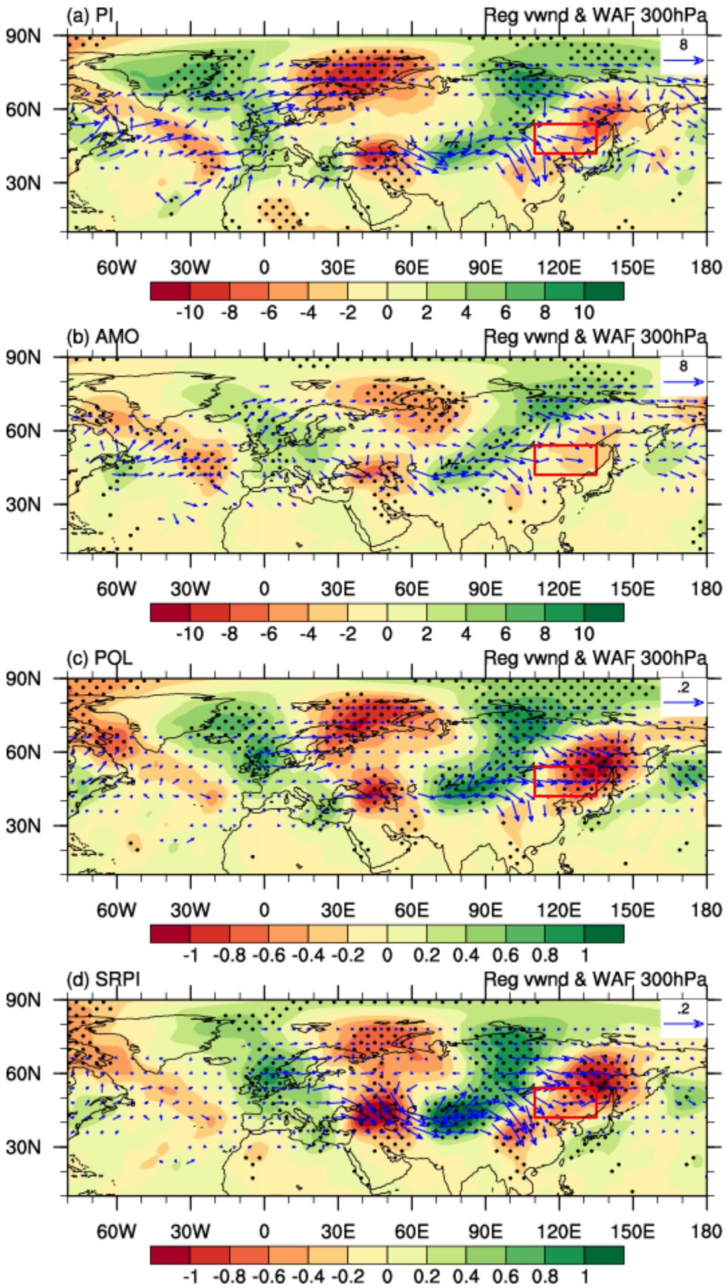

FIG. 10. Regression maps of 9-year low-pass filtered 300 hPa meridional wind anomalies (shading) and wave activity flux (vector; units: $m^2 s^{-2}$) in JA with regard to 9-year filtered (a) PINEC, (b) AMO index, (c) POL index, and (d) SRPI index during 1925–2010 after removing linear trend. Stippling denotes the anomalies significant at the 90% confidence level based on the Student's *t*-test. Here, PINEC is multiplied by –1.

Accepted for publication in *Journal of Climate*. DOI 10.1175/JCLI-D-19-0440.1.

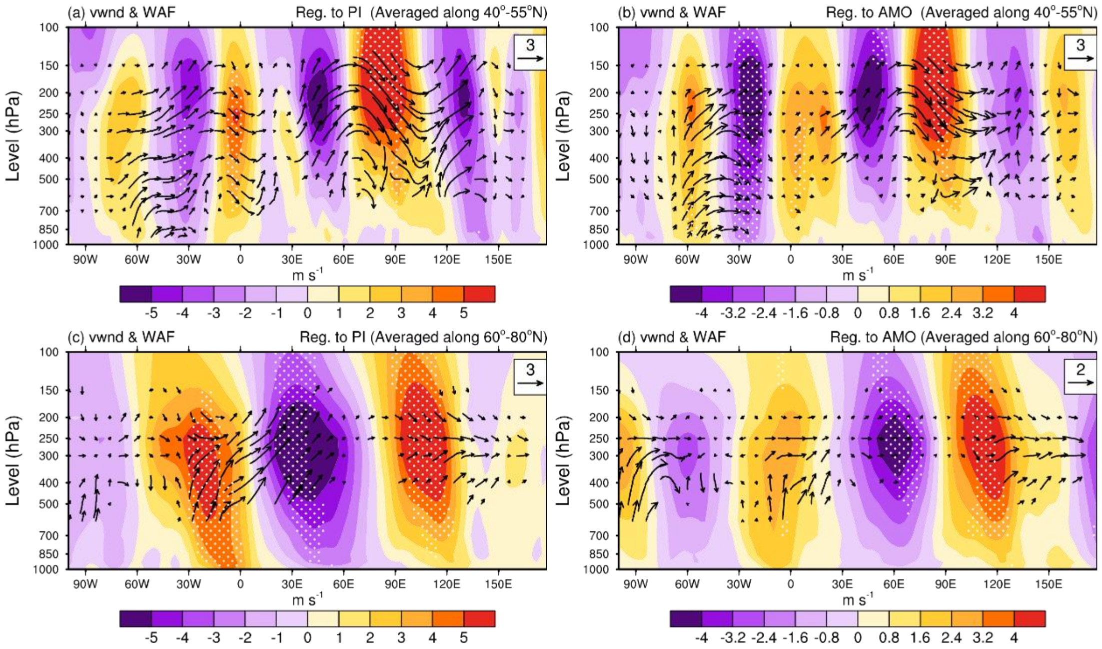

FIG. 11. Regression maps of 9-year low-pass filtered vertical-horizontal cross-section averaged along 40°N–55°N for JA wave flux (vectors, units: m s^{-1}) and meridional wind (shading, units: m s^{-1}) anomalies with regard to (a) 9-year filtered PINEC and (b) 9-year filtered AMO index. Regression maps of 9-year low-pass filtered vertical-horizontal cross-section averaged along 60°N–80°N for JA wave flux (vectors, units: m s^{-1}) and meridional wind (shading, units: m s^{-1}) anomalies with regard to (c) 9-year filtered PINEC and (d) 9-year filtered AMO index. Stippling denotes the anomalies significant at the 90% confidence level significant based on the Student's *t*-test. Here, PINEC is multiplied by –1.

Accepted for publication in *Journal of Climate*. DOI10.1175/JCLI-D-19-0440.1.

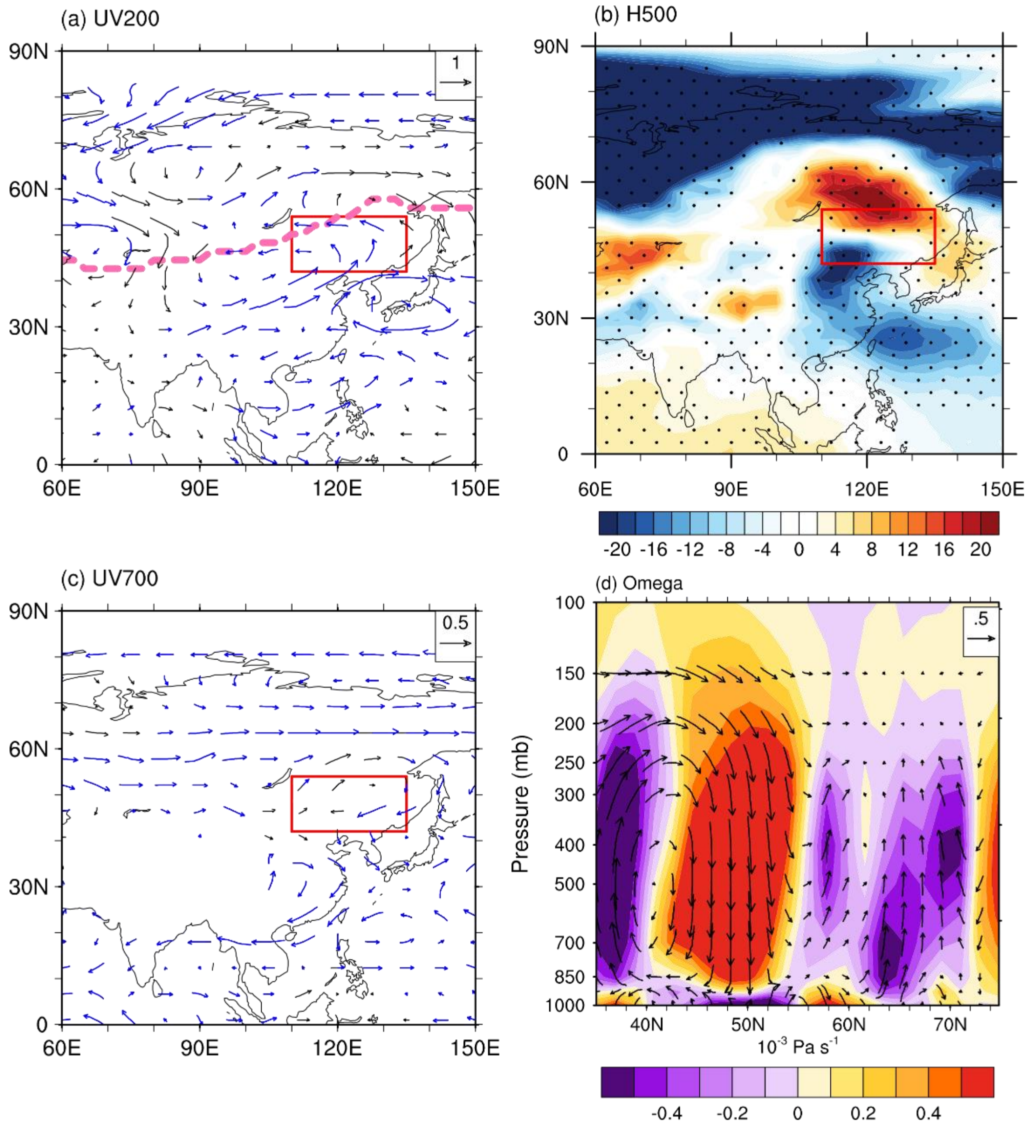

FIG. 12. Composite differences of (a) 200 hPa wind (units: m s^{-1}), (b) 500 hPa geopotential height (units: gpm), (c) 700 hPa wind (units: m s^{-1}), and (d) vertical–horizontal cross-section averaged along 115°–135 °E (units: m s^{-1}) between sensitive runs and control experiments based on 40 ensembles. Colored arrow in (a, c) and stippling in (b) denote that more than half of the models share the same sign as the ensemble mean. The dashed purple line in (a) gives the climatological position of the jet stream. Here, the zonal mean of geopotential height in (b) is removed.

Accepted for publication in *Journal of Climate*. DOI10.1175/JCLI-D-19-0440.1.

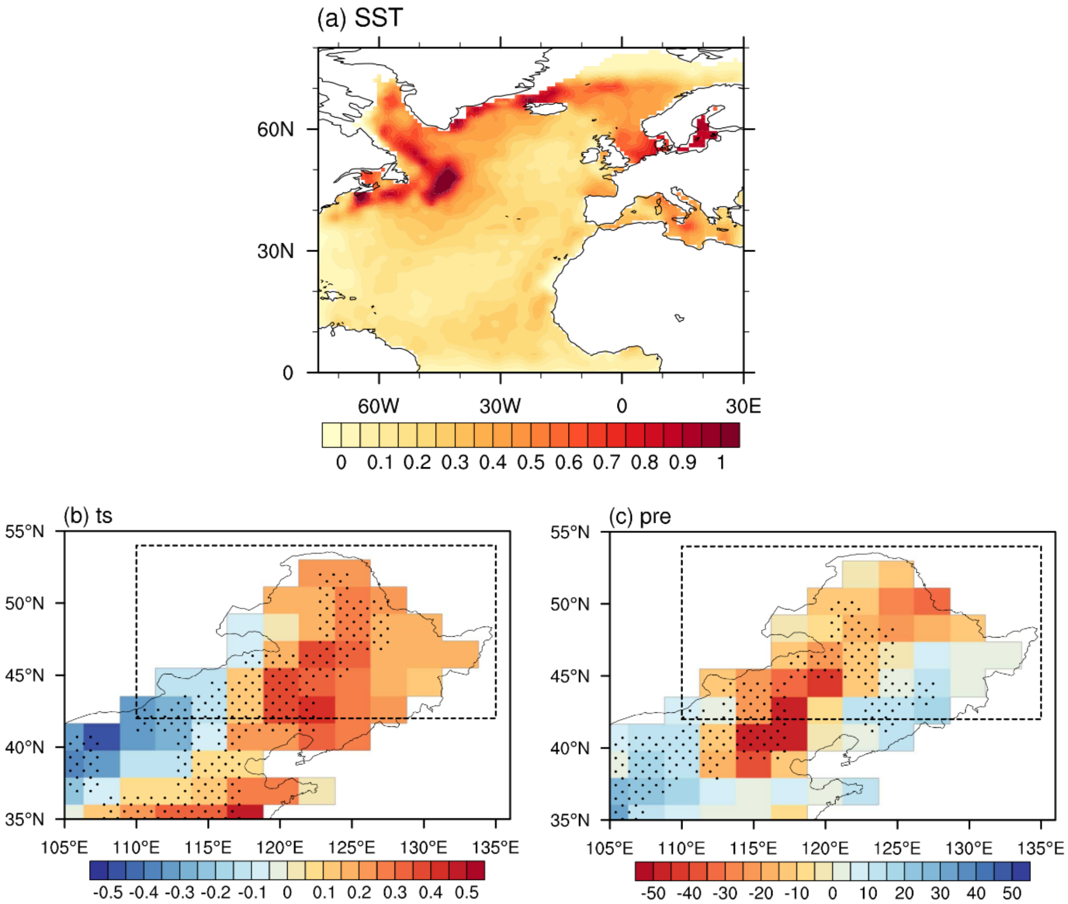

FIG. 13. Composite differences of (a) SST (units: °C), (b) surface air temperature (units: °C), and (c) precipitation (units: mm) between sensitive runs and control experiments based on the ensembles means of the 40 ensembles. Stippling in (b, c) denotes that more than half of the ensembles share the same sign as the ensemble mean.

Accepted for publication in *Journal of Climate*. DOI10.1175/JCLI-D-19-0440.1.